

Electronic structure of lattice relaxed alternating twist tNG -multilayer graphene: from few layers to bulk AT-graphite

Nicolas Leconte¹, Youngju Park¹, Jiaqi An¹, Appalakondaiah Samudrala¹, Jeil Jung^{1,2}

¹ Department of Physics, University of Seoul, Seoul 02504, Korea

² Department of Smart Cities, University of Seoul, Seoul 02504, Korea

E-mail: jeiljung@uos.ac.kr

Abstract. We calculate the electronic structure of AA'AA'... stacked alternating twist N -layer (tNG) graphene for $N = 3, 4, 5, 6, 8, 10, 20$ layers and bulk alternating twist (AT) graphite systems where the lattice relaxations are modeled by means of molecular dynamics simulations. We show that the symmetric AA'AA'... stacking is energetically preferred among all interlayer sliding geometries for progressively added layers up to $N = 6$. Lattice relaxations enhance electron-hole asymmetry, and reduce the magic angles with respect to calculations with fixed tunneling strengths that we quantify from few layers to bulk AT-graphite. Without a perpendicular electric field, the largest magic angle flat-band states locate around the middle layers following the largest eigenvalue eigenstate in a 1D-chain model of layers, while the density redistributes to outer layers for smaller magic twist angles corresponding to higher order effective bilayers in the 1D chain. A perpendicular electric field decouples the electronic structure into N Dirac bands with renormalized Fermi velocities with distinct even-odd band splitting behaviors, showing a gap for $N=4$ while for odd layers a Dirac cone remains between the flat band gaps. The magic angle error tolerance estimated from density of states maxima expand progressively from 0.05° in $t2G$ to up to 0.2° in AT-graphite, hence allowing a greater flexibility in multilayers. Decoupling of tNG into $t2G$ using effective interlayer tunneling proportional to the eigenvalues of a 1D layers chain allows to map tNG -multilayers bands onto those of periodic bulk AT-graphite's at different k_z values. We also obtain the Landau level density of states in the quantum Hall regime for magnetic fields of up to 50 T and confirm the presence of nearly flat bands around which suppressed density of states gap regions can develop by applying an electric field in $N > 3$ systems.

1. Introduction

Twisted graphene systems have emerged as the prime target and candidate for finding correlated electronic phenomena in 2D materials including flat band superconductivity [1, 2, 3, 4, 5, 6]. Research has expanded beyond the initial investigation of twisted bilayer graphene (t2G) [1] to include a variety of other layered moire materials that have shown hints of similar physics [7, 8, 9]. Alternating twist N -layer graphene (tNG) systems are particularly interesting for exploring correlation physics in light of recent experiments that have revealed flat band superconductivity for $N = 3, 4, 5$ systems [10, 3, 11].

In this work we studied the lattice relaxation effects in tNG systems by means of molecular dynamics calculations. The topmost layer was allowed to slide through the different stacking configurations in order to show that tNG with lowest total energies correspond to systems where local AA stacking are vertically aligned. We then mainly targeted our study on the largest magic angles for each tNG multilayer with most stable AA'AA'...-stacking and showed how the associated flat bands vary with experimental conditions like twist angle or tunneling strengths, electric fields and magnetic fields. In an effort to systematically improve prediction reliability and accuracy the relaxed atomic structures are obtained through real-space molecular dynamics calculations and the electronic structure analysis uses models that are informed by density functional theory [12].

The atomic relaxation is shown to affect the band structure by enhancing the asymmetry between the conduction and valence bands, separating the low energy bands from the higher bands at the Γ point as found in t2G, and allows to determine more clearly the flat band magic angles where the density of states (DOS) become maximum. From DOS calculations we observe a small decrease in the actual magic angle values when the relaxation effects are considered. We show that the charge associated to the flat bands are preferentially located around the middle layers of tNG for the largest magic angles, following the eigenstates of a 1D chain model of layers whose associated eigenvalues are proportional to the interlayer tunneling of effective bilayers. The decomposition of tNG into effective bilayers allows a mapping between tNG and bulk alternating twist (AT) graphite at selected k_z values. In the presence of perpendicular electric fields we see energy split Dirac cones near K and K' points in the moire Brillouin zone in even- N multilayer systems while one unshifted Dirac cone remains in odd- N systems. This distinct even-odd behavior

allows the development of band gaps in a t4G system near its largest magic angles and a Dirac cone is expected at charge neutrality for odd number of layers. Based on Landau level density of states calculations for up to $N = 6$ layers and magnetic fields of up to 50 Teslas in the quantum Hall regime we show the existence of constant energy DOS peaks associated to the nearly flat bands, and suppressed DOS gapped regions for $N > 3$ systems when we apply electric fields that can decouple the different effective Dirac cones within the tNG.

The paper is organized as follows. In Sect. 2, we introduce the continuum and tight-binding Hamiltonian models used for our calculations. In Sect. 3, we discuss the energetic stability of the system, the reduction of the magic angle predictions due to relaxation effects, as well as other observations made based on the DOS and electronic band structure for zero and finite magnetic fields, and then we elaborate on the finite system to bulk mapping. The summary and conclusions are presented in Sect. 4.

2. Methods

Here we outline our calculation methods based on the continuum moire bands theory [13] with fixed interlayer tunneling parametrizations of Ref. [14], and real-space tight-binding calculations [15] using the atomic and electronic structure calculation methods proposed in Ref. [16].

2.1. Continuum model calculations

The continuum model Hamiltonian for tNG that we use is based on the moire bands theory for t2G [13] and extensions thereof [17] using the parametrization in Ref. [14] for unequal interlayer inter-sublattice and intra-sublattice tunneling constants ω and ω' . The Hamiltonian reads

$$\mathcal{H}_k = \begin{pmatrix} H_k^- & T(\mathbf{r}) & 0 & \dots \\ T^\dagger(\mathbf{r}) & H_{k'}^+ & T^\dagger(\mathbf{r}) & \dots \\ 0 & T(\mathbf{r}) & H_k^- & \dots \\ \vdots & \vdots & \vdots & \ddots \end{pmatrix} + \Delta\epsilon, \quad (1)$$

where the diagonal blocks contain each alternating \pm twist graphene layer's Dirac cones,

$$H_k^\pm = \hbar v_F \begin{pmatrix} 0 & \pi_k^\dagger e^{\mp i\theta/2} \\ \pi_k e^{\pm i\theta/2} & 0 \end{pmatrix}. \quad (2)$$

Here $\pi_k = \bar{k}_x + i\bar{k}_y$ where the momentum vector \bar{k} is measured from the rotated Dirac cones. We use the Fermi

velocity at a single Dirac cone to be $v_F = (\sqrt{3}a/2\hbar)|t_0| \approx 10^6$ m/s with the effective nearest hopping parameter $t_0 = -3.1$ eV and a graphene lattice constant $a = 2.46$ Å. The off-diagonal blocks are the interlayer tunneling between the twisted layers,

$$T(\mathbf{r}) = \sum_{j=0,\pm} e^{-i\mathbf{Q}_j \cdot \mathbf{r}} \left[\begin{array}{cc} \omega' & \omega e^{-i\phi_j} \\ \omega e^{i\phi_j} & \omega' \end{array} \right] e^{-i\mathcal{G}_j \cdot \boldsymbol{\tau}_s} \quad (3)$$

where $\phi_j = (2\pi/3)j$, $\mathbf{Q}_j = \text{Rot}_{\phi_j}([K\theta(0, -1)])$ connecting the two adjacent layers' Dirac points, where we use $K = 4\pi/3a$. The tunneling amplitudes of $\omega = \omega_{BA'} = t_1/3$ and $\omega' = \omega_{AA'} = (-0.1835t_1^2 + 1.036t_1 - 0.06736)/3$ are estimated from the EXX+RPA fitting values [14] with $t_1 = 0.36$ eV, and the different ω and ω' values reflect the effect of out-of-plane atomic relaxation. The \mathcal{G}_j that correspond to \mathbf{Q}_j are the reciprocal lattice vectors of the original graphene, and $\boldsymbol{\tau}_s$ denotes the relative sliding displacement before the rotation that we have applied for the topmost pair of layers. The bulk alternating twist AT-graphite Hamiltonian at k_z reduces to the following form where the interlayer tunneling matrix acquires a z-dependent phase term as follows

$$\mathcal{H}_{\mathbf{k}}(k_z) = \begin{pmatrix} H_{\mathbf{k}}^- & 2T(\mathbf{r}) \cos(k_z c_0) \\ 2T^\dagger(\mathbf{r}) \cos(k_z c_0) & H_{\mathbf{k}}^+ \end{pmatrix}, \quad (4)$$

with $c_0 = 3.35$ Å a constant interlayer separation distance, and we assume that the vertical size of a unit cell is $2c_0$. The last term in Eq. (1) captures the effect of an electric field as

$$\Delta\epsilon = \text{diag} \left(-\frac{N-1}{2}, -\frac{N-1}{2} + 1, \dots, +\frac{N-1}{2} \right) \cdot \frac{\Delta V}{N-1} \mathbb{1}. \quad (5)$$

Both intra- and interlayer relaxation affect the momentum-space tunneling amplitudes $\omega^{(\prime)}$ in Eq. (3). We estimate the deformed tunneling amplitudes to \mathcal{G}_j at

$$\begin{aligned} \omega_{XX'}(\mathcal{G}_j) &= H_{XX'}(\mathbf{K} : \mathcal{G}_j) \\ &= \frac{1}{A_M} \int_{A_M} d\mathbf{r} \left[e^{i\mathcal{G}_j \cdot \mathbf{d}(\mathbf{r})} H_{XX'}(\mathbf{K} : \mathbf{d}(\mathbf{r})) \right] \end{aligned} \quad (6)$$

starting from the Wannier representation Bloch-band Hamiltonian $H_{XX'}(\mathbf{K} : \mathbf{d}(\mathbf{r}_i)) = \sum_j t_{ij}^{\text{inter}} e^{i\mathbf{K} \cdot \mathbf{r}_{ij}}$ [16, 17] where $X^{(\prime)}$ is A or B sublattice of bottom(top) layer and the interlayer hopping parameter t_{ij}^{inter} is defined in Eq. (9). The integration runs over a moire commensurate cell of area A_M , and we include both in-plane(\mathbf{u}) and out-of-plane(h) stacking deformation $\mathbf{d}(\mathbf{r}) = \mathbf{d}_0(\mathbf{r}) + \mathbf{u}(\mathbf{r}) + h(\mathbf{r})\hat{z}$ where $\mathbf{d}_0(\mathbf{r})$ is the rigid relative stacking information [18].

2.2. Tight-binding calculations

The tight-binding (TB) Hamiltonian in the basis $|i\rangle$ of localized states at site i is given by [19]

$$\hat{H} = \sum_i \epsilon_i |i\rangle \langle i| + \sum_{i,j} t_{ij} |i\rangle \langle j| \quad (7)$$

with eigenfunctions

$$|k\rangle = \frac{1}{\sqrt{n_{at}}} \sum_j^{n_{at}} e^{i\mathbf{k} \cdot \mathbf{r}_j} |j\rangle \quad (8)$$

with n_{at} the number of atoms and where $\mathbf{k} = (k_x, k_y)$ for the 2D systems and $\mathbf{k} = (k_x, k_y, k_z)$ for the bulk calculations. The ϵ_i are the onsite energies provided by the F2G2 model of graphene [20] that can additionally take potential energy shifts due to an electric field as in Eq. (5). The hopping terms $t_{ij} = t_{ij}^{\text{intra}} + t_{ij}^{\text{inter}}$ consist of intralayer t_{ij}^{intra} terms given by the F2G2 model and the interlayer t_{ij}^{inter} distance-dependent model of Ref. [16] with a scaling parameter S that reads

$$t_{ij}^{\text{inter}} = S \exp \left[\frac{c_{ij} - p}{q} \right] t_{\text{TC},ij}^{\text{inter}} \quad (9)$$

where S controls the magic angle value and $p = 3.25$ Å and $q = 1.34$ Å control the interlayer distance-dependent fitting of the tunneling at the K-point and

$$t_{\text{TC},ij} = V_{pp\pi}(r_{ij}) \left[1 - \left(\frac{c_{ij}}{r_{ij}} \right)^2 \right] + V_{pp\sigma}(r_{ij}) \left(\frac{c_{ij}}{r_{ij}} \right)^2 \quad (10)$$

where

$$V_{pp\pi}(r_{ij}) = V_{pp\pi}^0 \exp \left(-\frac{r_{ij} - a_0}{r_0} \right) \quad (11)$$

and

$$V_{pp\sigma}(r_{ij}) = V_{pp\sigma}^0 \exp \left(-\frac{r_{ij} - c_0}{r_0} \right) \quad (12)$$

with the interlayer distance $c_0 = 3.35$ Å, the rigid interatomic carbon distance in graphene $a_0 = 1.42$ Å, the transfer integral between nearest-neighbor atoms $V_{pp\pi}^0 = -2.7$ eV, the transfer integral between two vertically aligned atoms $V_{pp\sigma}^0 = 0.48$ eV, the decay length of the transfer integral set to $r_0 = 0.184a$ such that the next-nearest intralayer coupling becomes $0.1 V_{pp\sigma}^0$ and the magnitude of the interatomic distance $r_{ij} = |\mathbf{r}_{ij}|$. The cutoff for this distance-dependent model is finally set to 4.9 Å beyond which additional contributions do not affect the observables anymore [21]. The coefficient $S = 0.895$ in Eq. (9) is obtained using

$$S = \frac{\theta_1 |t_{\text{eff}}|}{\omega} s = C_1 s \quad (13)$$

where s contains the relaxation-specific effects and are calibrated to give the magic angle at $\theta_1 = 1.08^\circ$ using $t_{\text{eff}} = -3.1$ eV and $\omega = 0.11$ eV based on rigid bilayer graphene calculations [22]. In the so called continuum chiral model for multilayer tNG systems [23], where the same sublattice tunneling between consecutive layers is set to zero, the analytical flat band angles are given by

$$\theta^{(N)} = \omega / (v_F k_D \alpha_k^{(N)}) \quad (14)$$

through the dimensionless constant $\alpha_k^{(N)} = \alpha^{(2)} / \lambda_k$ for non-negative values of λ_k when $k = 1, \dots, N_e$ and $N_e = [N/2]$

is the number of t2G bilayers forming the alternating twist multilayer system such that $N = 2N_e$ for even-layered systems and $N = 2N_e + 1$ for odd-layered systems. The eigenvalues and eigenvectors of an N layers 1D-chain with unity hopping energy are given by

$$\lambda_k = 2 \cos(\kappa_k), \quad (15)$$

$$\psi_k(\ell) = \sqrt{\frac{2}{N+1}} \sin(\kappa_k \ell), \quad (16)$$

where $\kappa_k = \pi k / (N+1)$ and $\ell = 1, 2, \dots, N$ is the layer index.

For the electronic band structure calculations we construct commensurate cells that contain the smallest number of atoms whose moire period equals the period of the commensuration cell. Since the magic angle of a given system and the interlayer tunneling scaling parameter S' satisfy the relation $S'/\theta' = S/\theta$ the band flattening can be achieved at different physical magic twist angles if we modify the interlayer coupling strength. We use the scalability of the electronic structure with interlayer tunneling to calculate the band structure of a given effective twist angle θ_{eff} based on a commensurate reference twist angle θ_{ref} . The updates in S' for changes in $\delta\theta$, δv_F , or $\delta\omega$ parameters can be introduced through

$$S' = C'_1 s = C_1 \left(1 + \frac{\delta\theta}{\theta_{\text{ref}}}\right) \left(1 + \frac{\delta v_F}{v_F}\right) \left(\frac{\omega}{\omega + \delta\omega}\right) s. \quad (17)$$

and the electronic band structures at effective twist angles can be obtained through

$$\theta_{\text{eff}} = \theta_{\text{ref}} - \delta\theta = \frac{S}{S'} \theta_{\text{ref}} \quad (18)$$

where θ_{ref} is a commensurate superlattice angle close to the value of the effective θ_{eff} that we want to calculate. The specific choice of S' for each system is summarized in Table B1 from the Appendix that minimizes the bandwidth

$$W_\Gamma = E_{\text{cond}}(\Gamma) - E_{\text{val}}(\Gamma) \quad (19)$$

that we defined subtracting the maximum of the lowest conduction band and the minimum of the highest valence band at the Γ -point. We verified that our estimate of the magic angle remains the same if we choose the valence band reference value to be at the M-point. For most of the quantitative magic angle analysis presented in Sect. 3.2 we have based our band flatness criterion instead on the DOS maxima peaks as a function of θ thus leading to small differences for θ_{eff} obtained from the electronic band structures and the DOS-inferred θ -values among E values near charge neutrality

$$\theta_M = \text{argmax}_\theta \text{DOS}(E, \theta). \quad (20)$$

The DOS calculations have been carried out through direct diagonalization when allowed by the system sizes and by using the Lanczos method when we need to calculate very large systems with millions of atoms

$$\text{DOS}_\eta(E) = -\frac{1}{\pi} \Im m \left\langle \varphi_{RP} \left| \frac{1}{E + i\eta - \tilde{H}} \right| \varphi_{RP} \right\rangle \quad (21)$$

where RP refers to a random phase being used to approximate the trace of large matrices [24] and η is the broadening factor that allows to control the energy resolution. We finally note that for the magnetic field calculations, we use a Peierls phase substitution in the hopping terms as discussed in Ref. [25].

2.3. Molecular dynamics simulations

The value $S = 0.895$ used in Eq. (9) as well as the modified S' values from Eq. (17) are suitable when using the REBO2 force-field [26] for the intralayer interactions and the EXX-RPA-informed [12] DRIP [27] interlayer potential when performing the MD calculations. Specifically, we performed the MD calculations using LAMMPS [28] with the FIRE minimization scheme [29] with a time step of 0.001 ps and a stopping tolerance on the forces of 0.001 eV/Å. Interlayer interactions are only included between adjacent layers. We note that the band separation between the flat bands and the rest of the spectrum is over-estimated when using the present REBO2 potential [16], while better mechanical predictions can be obtained using the computationally more demanding GAP₂₀ potential [30].

3. Atomic and electronic structure of tNG

The alternating twist tNG multilayers with equal twist angle magnitudes give rise to moire patterns at each interface that have the same period and whose angles are aligned. The resulting moire patterns can still have different interlayer stacking but here we focus our atomic and electronic structure study mainly on the properties of AA'AA'... structures where all graphene layers are exactly on top of each other before rotating the layers, based on the energetic considerations from Sect. 3.1.

3.1. Sliding energetics

Electronic structure studies presented so far have often modeled the simplest AA'AA'... structure for tNG in Fig. 1a. that does not have any sliding between consecutive layers. Calculations of sliding energetics for t3G based on molecular dynamics (MD) calculations have shown indeed this is the case for trilayers [31]. Here, we extend the calculations for aligned moire angles but variable sliding geometries for tNG multilayers of up to $N = 6$ layers and verify that a similar behavior takes place for multilayers beyond $N = 3$. In our setup we assume that $N = 1$ up to $N - 1$ do not include any sliding while layer N is translated by τ with respect to layer $N - 2$ in the usual AA, AB, and BA configurations in Fig. 1b.. The corresponding energetics are illustrated in panels c., d., e. and f.. In Fig. 1c. we show the total structural energy per atom as a function of stacking for t3G and set the AA-stacking energy at zero. Comparison between the total energies of rigid (dashed-dotted green), in-plane only (dashed orange) and fully relaxed (solid blue)

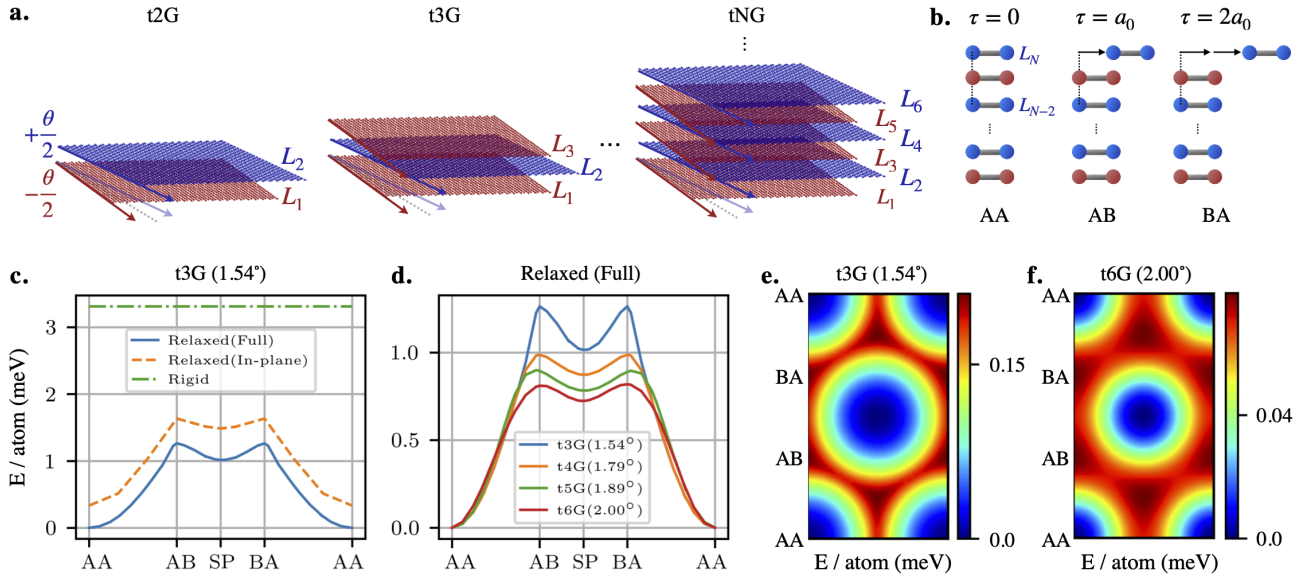


Figure 1. (color online) **a.** Schematic of alternating twist t2G, t3G, t6G multilayers and beyond numbered from bottom to top. The $\mp\theta/2$ alternating twists are shown around a given reference axis represented in gray. **b.** Sliding vectors τ prior to twisting the layers define the local stacking. We always slide the uppermost layer N with respect to layer $N-2$ through AA, AB and BA stackings defined in the same way as non-twisted bilayer graphene systems. **c.** Energy per atom for the t3L system where we gradually include additional degrees of freedom from the rigid (dashed-dotted green) to the in-plane relaxed system (dashed orange) and the fully relaxed system (solid blue). We set the energy of the AA stacking of the fully relaxed system to zero. **d.** Comparison of the fully relaxed structures with respect to sliding when increasing the number of layers. The angles corresponding to each curve are the ones used for the smallest commensurate cell close to the one of the magic angle of each system, *i.e.* $\theta_{\text{cell}} = 1.54, 1.79, 1.89$ and 2.00° , respectively. For all systems, the most stable AA structure corresponds to the situation where layer N has zero sliding τ with respect to layer $N-2$. The panels **e.** and **f.** correspond to the same data as panel **d.** but for the full sliding range, for t3G and t6G respectively.

systems indicates that the largest energy gain happens thanks to the reduction of potential energy when the atoms are allowed to rearrange along the in-plane direction. As expected, the rigid configuration does not show any sliding τ -dependence. The clear reduction in the total energy at the AA stacked regions for the fully relaxed system of about 1 meV/atom on average indicates that this stacking is favored vs the AB or BA or the intermediate saddle point SP stacking. The shape of the energy barriers of in-plane relaxation-only results are nearly the same as for the fully relaxed system, thus highlighting the relative unimportance of the stacking-induced corrugation of the layers, implying that the energy minimization of the additional graphene layers will mainly depend on the relative moire pattern sliding between the nearest two layers that form the commensurate patterns. In panel **d.** we show similar τ -dependent total energies for $N = 3, 4, 5$ and 6 layers-tNG at their respective magic angle twists. On the right panels in Fig. 1e. and f. we show this same total energy landscape as a 2D colormap for all possible slidings for the t3G and the t6G systems. Here, we see that the energetically unfavorable stackings can relax into the most stable AA'AA'... stacked system through an energy barrier-free path. We can gain insight about the relaxation process if we distinguish the total equilibrium interatomic energy by breaking it down into an elastic intralayer contribution that rises to resist deformation,

and the potential interlayer interaction that reduces the total energy of the system by accommodating to the lowest energy stacking. In the MD calculations the elastic and potential energy contributions can be obtained during postprocessing, see Eqs. (A.1, A.2) for their definitions in the Appendix. We note that for the AA stacking the total energy reduction due to the potential energy minimization can become almost an order of magnitude more important than the elastic energy penalty, see Fig. A1 in the Appendix for illustration on t3G and t4G and further discussions on characteristic sublattice dependent chiral signatures. For the total potential energy map, the AA stacking shows the highest binding energy, or conversely the lowest free energy; the energetically favorable and unfavorable regions can thus be fully inferred from the potential energy maps.

3.2. Magic angles based on DOS calculations

Here we find the numerical magic angle predictions of realistic lattice relaxed tNG systems that include both intra- and inter sublattice interlayer tunneling and using tight-binding calculations. Due to computational limitations when performing exact diagonalization to obtain the electronic band structure we use Lanczos recursion methods that allows to efficiently obtain the DOS on arbitrarily large systems with tens of million atoms which allows us

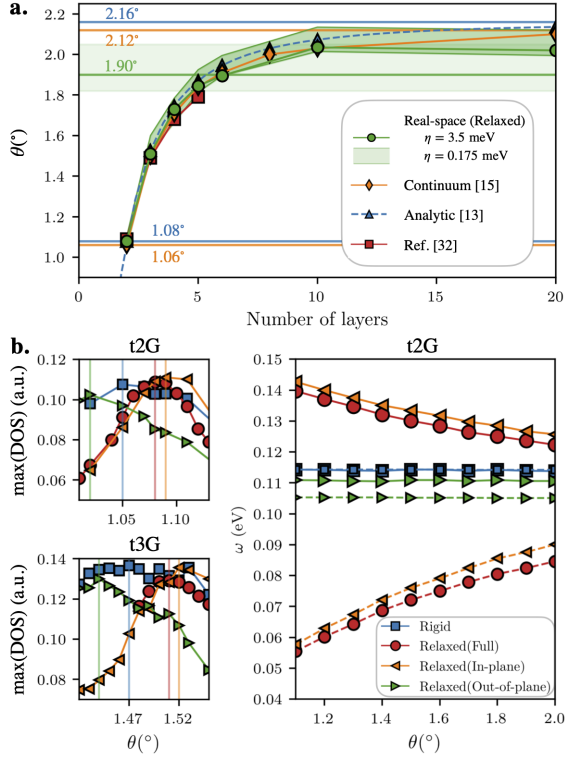


Figure 2. (color online) **a.** Magic angles as a function of layer number N from calculations based on our lattice relaxed (green), lattice rigid (purple), fixed tunneling continuum (orange) from Ref. [14], fixed tunneling analytic (blue) from Ref. [23], and relaxed continuum model (red) from Ref. [32]. Analytically predicted values of the largest magic angles are obtained from the magic angle hierarchy from Ref. [23] using Eq. 14 and our numerically calculated values are obtained using large scale DOS calculations using Eq. 21. The green-shaded horizontal line and region correspond to the $\eta = 3.5$ and $\eta = 0.175$ meV bulk AT-graphite predictions from the real-space calculations. We refer to Figs. B1 regarding the method used to extract the values reported in this figure. **b.** t2G (upper-left) and t3G (lower-right) magic angle predictions for the rigid (blue), in-plane-only relaxed (orange), out-of-plane-only relaxed (green) and fully relaxed configurations (red) where the vertical lines indicate the magic angle as predicted by the maxima of the $\max(\text{DOS})$ curves defined in a manner similar to Fig. B1. (right) The estimated ω_{AB} (solid) and ω_{AA} (dashed) by Eq. (6) as a function of twist angle θ . We observe that the main contribution to the predictions from the fully-relaxed calculations comes from the in-plane relaxation where the corresponding lattice reconstruction becomes weaker with increasing twist angle hence providing grounds for the reduction of the magic angle with respect to the analytical predictions based on the constant tunneling from the reference t2G system, as observed in panel **a.**

to probe a fine grid of commensurate angles, linking the magic-angle flat bands to maxima in the DOS as a function of twist angle. We specifically focus on the first magic angle of tNG denoted as $\theta_1^{(N)}$ that from here onwards we refer to as simply magic angle. We have scanned the relaxed geometries at steps of approximately $\Delta\theta \sim 0.005^\circ$. The real space Hamiltonian includes both intra and inter sublattice interlayer tunneling as well as the lattice relaxation effects unlike the analytical model that only has inter-sublattice tunneling for rigid lattices. The DOS peaks show a well defined maximum when we allow a sufficiently large

broadening $\eta \sim 3.5$ meV, which is smaller but comparable to the bandwidths of the low energy nearly flat bands of typically ~ 20 meV, see Fig. B2 for t3G in the Appendix for a comparison between the electronic band structure and the corresponding features in the DOS using exact diagonalization. In our Lanczos calculations we have used two different broadening values to identify the magic angles. The width of the DOS peaks indicates the uncertainty in the magic twist angle values where experimental strong correlations are expected. Using a smaller $\eta \sim 0.175$ meV we can resolve finer undercover peaks within this broader peak that reflects the fine band structure features buried within a single nearly flat band. This behavior allows to define a *range of magic twist angles* centered around a value rather than a sharply defined unique magic angle value as we commonly understand. This is illustrated respectively for large and smaller broadening in Figs. B1 of the Appendix for t2G up to t20G and AT-graphite expanding on earlier discussions on t2G presented in Ref. [16]. In Table. 1 and Fig. 2 we compare the magic angles obtained from the real space numerical calculations against a tNG continuum model with fixed interlayer tunneling as parametrized in Ref. [14]. Provided that the interlayer tunneling model

N	Real-space relaxed	Continuum [14]	Ref. [23]	Ref. [32]
2	1.080	1.06	1.08	1.09
3	1.510	1.49	1.527	1.49
4	1.730	1.70	1.748	1.68
5	1.845	1.84	1.871	1.79
6	1.895	1.91	1.946	
10	2.035	2.03	2.07	
20	2.020	2.08	2.136	
Bulk	1.90	2.12	2.16	

Table 1. Supporting numerical data for Fig. 2. In the real-space relaxed calculations in the second column obtained using $\eta = 3.5$ meV we see a reduction of the magic angle value θ with respect to the continuum model values with fixed interlayer tunneling in the third column as we progressively increase the number of layers N and hence the respective first magic angles. We include as reference the predictions of the analytical values [23] and continuum relaxed models [32] in columns four and five.

remains the same, the magic angle $\theta_1^{\text{bulk}} = 2\theta_1^{(2)}$ in the limit of infinite N bulk AT-graphite systems is expected to be twice the value for t2G, namely $\theta_1^{(2)} = 1.08^\circ$, since we have two interacting interfaces per unit cell as noted in Eq. (4). The numerical magic angles resulting from lattice relaxed calculations using a broadening of $\eta = 3.5$ meV in Eq. (21) shows smaller magic angles such that $\theta_1^{\text{bulk}} < 2\theta_1^{(2)}$, with the large $N = 20$ magic angle going as low as $\theta_1^{(20)} = 2.02^\circ$ and the AT-graphite limit dipping all the way down to $\theta_1^{\text{bulk}} = 1.9^\circ$. Similarly, a wider range of magic angles can be identified in the DOS peaks when we use the smaller $\eta = 0.175$ meV broadening.

We observe a gradual decrease of the numerical magic

angle with respect to the fixed interlayer coupling continuum model with increasing number that can be understood from an effective reduction of interlayer tunneling strength we discuss in the following. The evolution trend of the magic angles with lattice relaxations can be understood paying attention to its relationship with the interlayer tunneling in few layers systems, particularly t2G, keeping in mind that the magic angle will increase when the integrated interlayer tunneling ω between unequal sublattice sites between contiguous layers becomes larger. In Fig. 2 **b**, we show the comparison of the magic angles obtained for rigid systems with a fixed interlayer equilibrium distance of $c_0 = 3.313 \text{ \AA}$, corresponding to AB or BA stacking interlayer distances of untwisted bilayer systems using our EXX-RPA force fields, the in-plane-only relaxed with the same c_0 , the out-of-plane-only relaxed, and the fully relaxed geometries for t2G that reveal the different elements entering the interlayer tunneling that affect the magic angle values. Because the interlayer distance of the rigid model (blue) is set to the shortest local interlayer equilibrium distance that maximizes tunneling, it is natural to expect that the predicted magic angle is larger than the out-of-plane relaxed (green) case that separates further the average interlayer distance between layers. The in-plane relaxed (orange) case that keeps the same interlayer distance as the rigid systems shows the largest magic angles. This behavior indicates that the surface-integrated inter-sublattice interlayer tunneling ω is effectively enhanced thanks to the increase of AB and BA local stacking areas when in-plane strains are allowed. Then a full relaxation that includes the out-of-plane corrugations will increase the average interlayer distance, reducing in turn the interlayer tunneling and therefore the magic angle. Using an electronic and atomic structure model calibrated to have a magic angle of 1.08° [16] for the fully relaxed system we observe that the rigid t2G's magic angle is 1.05° , the in-plane-relaxation enhances it to 1.09° , and an out-of-plane relaxation reduces it down to 1.02° . Likewise for t3G we see a similar trend of 1.47° , 1.52° and 1.44° respectively for fully relaxed, in-plane only and out-of-plane only. We can thus conclude that the drop in magic angle with respect to the continuum fixed interlayer tunneling model of the lattice relaxed tNG model for increasing N is mainly because of the progressive decrease of in-plane strains for larger θ , and therefore of interlayer tunneling ω between different sublattice atoms in contiguous layers.

We note that in the bulk limit we have an additional ingredient that enhances the drop in the magic twist angle value to 1.9° because the periodicity along the z -axis implies that all layers are modeled to be flat and are free of corrugation. In this limit the equilibrium interlayer distance predicted by our EXX-RPA informed force field on the 2.00° twist angle used to perform the calculations has a constant interlayer distance value of 3.328 \AA that is slightly larger than the AB-stacking value of 3.313 \AA of untwisted bilayers used for the rigid calculations of our tNG models.

This larger interlayer distance of rigid AT-graphite reduces the inter-layer coupling strength and therefore results in a decrease of the predicted magic angle when compared to finite multilayer systems.

To further clarify the evolution of interlayer separation when transitioning from finite tNG systems to the AT-graphite bulk we present the average interlayer distance as a function of twist angle θ and number of layers N in the Appendix. Intuitively we can understand this behavior from the fact that the AA stacking regions, that have the farthest local equilibrium interlayer separation, increases with twist angle. On the other hand, the corrugations are expected to gradually decrease for increasing number of N . In terms of the angle-dependence in Fig. C1, we observe that the average and constant bulk interlayer distances increase with twist angle. Using the recipe to assign a specific local stacking to each atom in a twisted relaxed system introduced in Ref. [16], and using the respective area ratio of these stackings, we can predict the bulk interlayer distance trend using Eq. (C.1). We finally observe that the free-standing t2G counterpart produces a similar increasing trend with twist angle but with slightly larger interlayer distances thanks to the presence of out-of-plane corrugations. We show in Fig. C2, for $\theta = 2^\circ$, the N -dependence of a tNG system that converges monotonically to the bulk inter-layer distance when we use the simplifying constraint of keeping the outer-layer atoms in the same xy plane to remove the corrugations. Without this constraint, in the fully relaxed system, the average interlayer distances converge more slowly to the bulk behavior as a function of N , showing a local minimum at around $N = 14$. This behavior is in qualitative agreement with the maximum seen for $N = 10$ in Fig. 2.

3.3. Electronic band structures of tNG multilayers and Hofstadter butterflies

In the following we discuss the effects of lattice relaxation in the electronic band structures of tNG systems. For representation convenience the band structures are plotted in the Brillouin zones of smallest superlattice geometries whose periods are coincident with those of moire patterns. Because this type of coincidence only happens at discrete twist angle sets that are separated from each other we update the original interlayer tunneling prefactor S in Eq. (9) to S' of Eq. (17) to calculate the effective twisted angle θ_{eff} given in Eq. (18). The criterion to define the flattest band is based on the minimization of the band width at the Γ -point, leading to slightly different values than the experimentally more relevant ones predicted from DOS calculations in Sect. 3.2. We thus refer to the magic angles represented in the electronic band structure calculations as θ_{eff} and the ones from the DOS calculations as simply θ . The band structures of t3G up to t6G are shown in Fig. 3 both for the continuum model with fixed interlayer interactions and lattice-relaxed real space tight-binding calculations, the latter with and without perpendicular electric fields. The

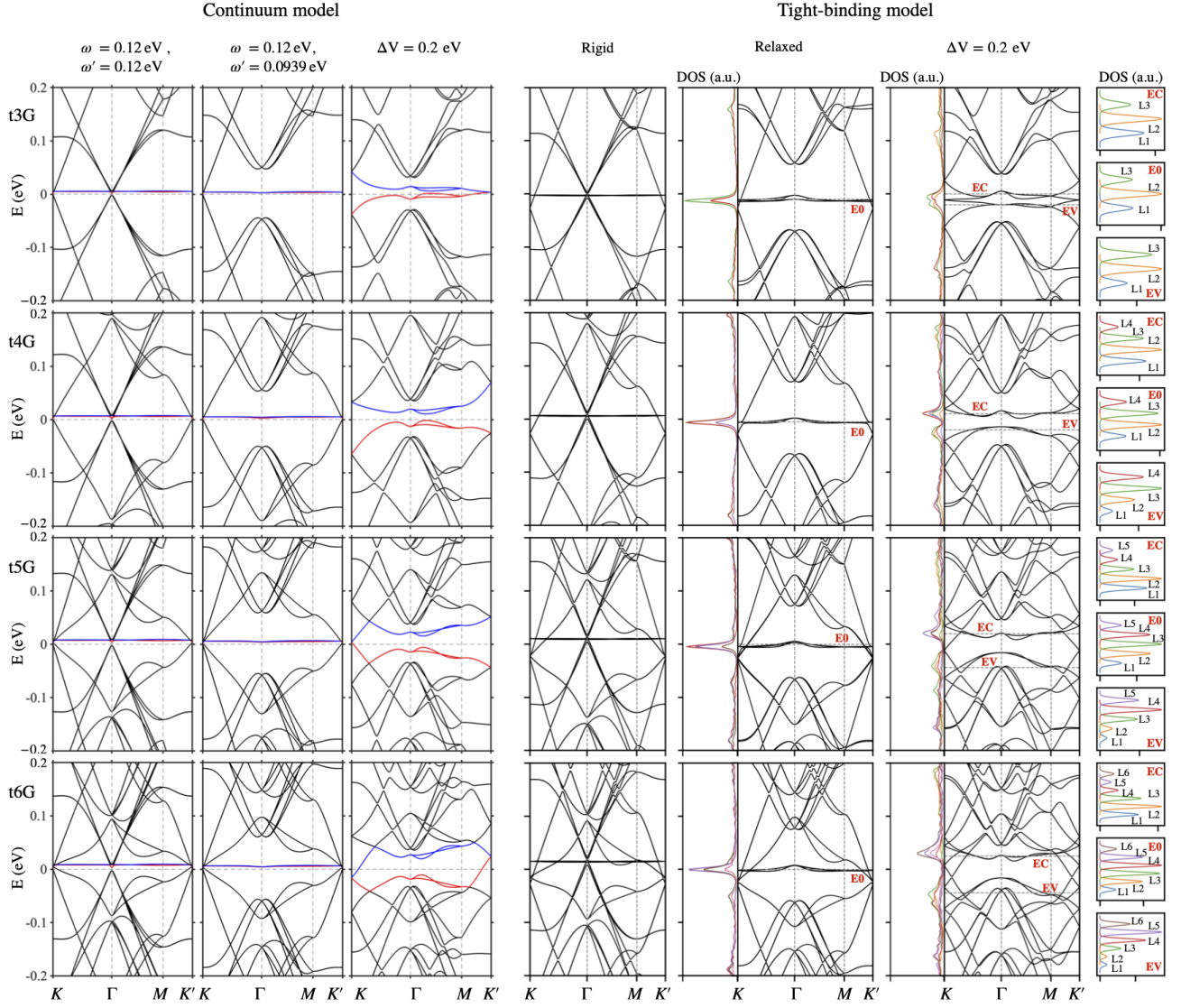


Figure 3. Electronic band structure of tNG for $N = 3$ up to $N = 6$ for the magic angles based on the criterion of minimizing the bandwidth at the Γ -point leading to values of $\theta_{\text{eff}} = 1.51^\circ, 1.72^\circ, 1.84^\circ$ and 1.9° respectively, where we illustrate the lattice relaxation and perpendicular electric field effects. These values are only slightly different from the experimentally more relevant magic angle predictions θ based on the criterion of maximizing the DOS from Fig. 2 and Table 1 and these differences have a negligible impact on the conclusions drawn from this figure. The physical commensurate angles θ_{cell} and S' parameters from Eq. 17 that are used to simulate current effective angles θ_{eff} are listed in Table. B1. *Left panel:* Continuum model electronic bands at the K -valley. The left most column shows the equal tunneling $\omega' = \omega = 0.12$ eV rigid model bands and distinct $\omega' = 0.0939$ eV, $\omega = 0.12$ eV tunneling that partially accounts for out of plane lattice relaxation effects. The interlayer potential modified bands on top of this relaxed model illustrated in the third column shows the splitting into N Dirac cones manifest at the K and K' points in the moire Brillouin zone. *Right panel:* The electronic band structures for the rigid and relaxed systems at twist angles with maximum flatness of the central bands corresponding to bandwidth minima at the Γ -point. Contrary to the continuum bands, the lattice calculations show simultaneously both valleys K and K' . The layered-resolved DOS indicates that the states corresponding to the flat bands are located preferentially at the central layers of the system. Comparison between rigid and relaxed structures illustrates the overall electron-hole symmetry breaking introduced by the relaxation effects and opening of band gaps at the Γ point. The interlayer potential difference $\Delta V = 0.2$ eV between top and bottom layers, see Eq. (5), that can be introduced by a perpendicular electric field tends to broaden the bandwidth of the low energy bands. The 4-layers system uniquely shows a bandgap in the electronic band structure, and the layer-resolved DOS show that the electric-field induced degeneracy-lifted low energy bands are leading to layer resolved charge polarization where we label the layers from bottom to top from L1 to L6 as defined in Fig. 1.

relaxation separates the high energy bands at Γ from the low energy bands [33] and introduces an electron-hole asymmetry that becomes more pronounced in the tight-binding calculations. The layer-resolved density of states for each of these systems show that the flat band states are primarily populated by electrons associated with the atoms in the inner layers. When applying an electric field to these systems in Fig. 3, we notice that the layer-resolved DOS in the side-panels induces an electron-hole asymmetry in the degeneracy lifted flat band where the electron states are mostly located at the bottom layers while the hole states are being pushed towards the top layers. The corresponding band structures confirm the expected hybridization between the Dirac bands and the flat bands and, quite notably, show a clear real gap in the case of the t4G system [32]. The t5G system sees a robust crossing of the t4G gap by a Dirac cone at the K-point, while the t6G system sees two such crossing bands. We further illustrate the gap opening predicted for the systems with $N \leq 6$ by calculating the Landau level density of states diagrams up to 50 T for each of the systems in Fig. 4. We indicate with dashed and dashed-dotted lines the location of the flat band and zeroth Landau level of (one of the) Dirac cones, respectively. The well-resolved separation and the suppressed density of states regions reveals that the flat bands are energy-pinned in the quantum Hall regime in $N > 3$ systems. This effect can be verified when we apply electric fields that can decouple the effective Dirac cones and flat band contributions as observed in the band structures of Fig. 3.

3.4. From finite tNG multilayers to bulk AT-graphite bands

Here, we discuss the electronic structure of tNG finite stacks in relation to bulk AT-graphite bands in the limit of $N \rightarrow \infty$. Specifically, we verify the mapping of tNG bands onto those of bulk AT-graphite with different k_z . This mapping can be achieved by relating the eigenvalues of a nearest neighbor linear 1D-chain of layers in a tNG system with the interlayer tunneling values of effective t2G systems it is made of. The preference of charge accumulation in the middle layers for the magic angle bands shown in Fig. 3 follows the wave function structure of the largest eigenvalue eigenstate of this 1D-linear chain, and therefore outer layer charge accumulation will be favored for smaller magic angles corresponding to reduced tunneling effective twisted bilayers. We start by briefly discussing the decomposition of tNG bands into a sum of twisted bilayer models at different twist angles, plus a single layer for odd number of layers, that were obtained through singular value decomposition of the layers hopping matrix where odd and even layers were distinguished in Ref. [23]. It turns out that this decomposition follows from the same type of basis change used to express a Bernal stacked N -multilayer graphene in terms of $[N/2]$ effective bilayers with renormalized interlayer tunneling values, plus a single layer graphene for odd N [34]. We denote as $\psi_k(\ell)$ the layer resolved

wave function amplitudes of the eigenstates $|\psi_k\rangle$ where $\ell = 1, 2, \dots, N$ are the layer indices. The tNG multilayer Hamiltonian can be decomposed into smaller subsystems by choosing an appropriate basis of odd layer symmetric or even layer antisymmetric wave functions based on the eigenstates of opposite sign eigenvalues $\lambda_k = -\lambda_{N+1-k}$

$$\begin{aligned} |\tilde{\psi}_k^{\text{odd}}\rangle &= \frac{|\psi_k\rangle + |\psi_{N+1-k}\rangle}{\sqrt{2}}, \\ |\tilde{\psi}_k^{\text{even}}\rangle &= \frac{|\psi_k\rangle - |\psi_{N+1-k}\rangle}{\sqrt{2}}. \end{aligned} \quad (22)$$

with $k = 1, 2, \dots, N_e$. When N is odd and $k = N_o$ we have for the zero eigenvalue state $|\tilde{\psi}_k^{\text{odd}}\rangle = |\psi_k\rangle$. The eigenstates corresponding to the k^{th} eigenvalue following Eq. (16) and the associated symmetric/antisymmetric forms are shown in Fig. D1 in the appendix. This figure shows the preferential accumulation of charge in the middle layers for $k = 1$ and how the charge progressively redistributes towards the outer layers for larger k , or equivalently for the magic angles of the second or third effective bilayers.

If we represent the Hamiltonian given in Eq. (1) in this modified basis that distinguishes odd and even layers we get

$$\tilde{\mathcal{H}}_k^{(\text{dec})} = \begin{pmatrix} h_{oo}^{AA} \mathbf{1}_o & h_{oo}^{AB} \mathbf{1}_o & T_{oe}^{AA} \Lambda & T_{oe}^{AB} \Lambda \\ h_{oo}^{BA} \mathbf{1}_o & h_{oo}^{BB} \mathbf{1}_o & T_{oe}^{BA} \Lambda & T_{oe}^{BB} \Lambda \\ T_{eo}^{AA} \Lambda & T_{eo}^{AB} \Lambda & h_{ee}^{AA} \mathbf{1}_e & h_{ee}^{AB} \mathbf{1}_e \\ T_{eo}^{BA} \Lambda & T_{eo}^{BB} \Lambda & h_{ee}^{BA} \mathbf{1}_e & h_{ee}^{BB} \mathbf{1}_e \end{pmatrix}. \quad (23)$$

We can further transform the matrix into effective t2G-like Hamiltonian diagonal blocks with tunneling strengths proportional to the eigenvalue λ_k by further grouping the basis into alternating sublattices for different layers

$$\begin{aligned} \mathcal{H}_k^{(\text{dec})} &= P \tilde{\mathcal{H}}_k P^\dagger \\ &= \mathcal{H}_{k\lambda_1}^{(t2G)} \oplus \mathcal{H}_{k\lambda_2}^{(t2G)} \oplus \dots \oplus \mathcal{H}_{k\lambda_{N_e}}^{(t2G)} \\ &\quad \left(\oplus \mathcal{H}_k^{(1G)} \right) \end{aligned} \quad (24)$$

as discussed in Refs. [34, 23]. Here P is the transformation matrix that takes the sublattice $s = A, B$ labeled basis $(\psi_{A_1}, \psi_{B_1}, \psi_{A_2}, \psi_{B_2}, \dots, \psi_{A_N}, \psi_{B_N})^T$ to $(\psi_A^o, \psi_B^o, \psi_A^e, \psi_B^e)^T$ where $\psi_s^o = (\psi_{s_1}, \psi_{s_3}, \dots, \psi_{s_{2N_o-1}})^T$ and $\psi_s^e = (\psi_{s_2}, \psi_{s_4}, \dots, \psi_{s_{2N_e}})^T$ where $N_{o/e}$ is the number of odd/even layers. The $\Lambda = \sum_k \lambda_k \delta_{k,n}$ are diagonal $N_o \times N_e$ matrices with $n, k = 1, 2, \dots, N_e$. A detailed derivation of the decomposition procedure following the basis change is presented in Appendix D. From Eq. (4) the bands of bulk AT-graphite can be viewed as standing wave bilayer bands with renormalized interlayer tunneling strengths with periodic boundary conditions and therefore the few layers graphene bands can be related with those of bulk graphite at select k_z by

$$k_z c_0 = \frac{\pi k}{N+1} \quad (25)$$

where we require the interlayer tunneling for bulk AT-graphite Eq. (4) and the effective bilayer Hamiltonian

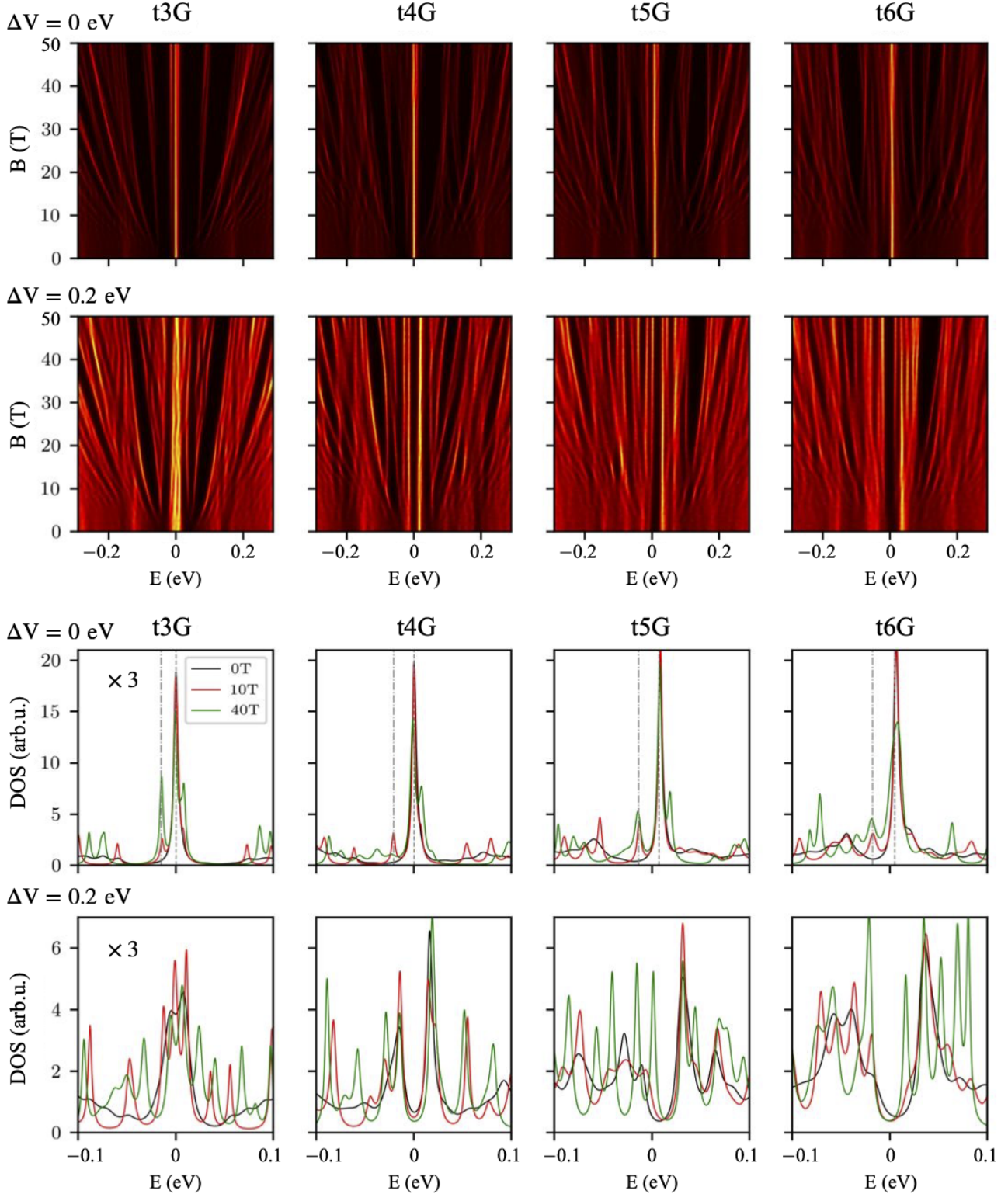


Figure 4. (color online) Hofstadter Landau level maps based on the DOS (top) and DOS curves at selected magnetic fields (bottom) for tNG with $N = 3, 4, 5, 6$ with and without $\Delta V = 0.2$ eV top-bottom potential energy difference as defined in Eq. (5). The angles θ_{eff} are the same ones as in Fig. 3 for which the physical commensurate angles and S' parameters are listed in Table. B1. The amplitude of the t3G DOS curves have been multiplied by three to match the scale of the $N > 3$ systems that have higher flat band peaks. The $N = 3$ system doesn't show signs of a band gap in the presence of an interlayer potential difference while for the other N considered the electric field-induced band gap due to DOS suppression in the quantum Hall regime increases with number of layers. The dashed vertical lines in the $\Delta V = 0$ DOS plots indicate the flat band energies and the zeroth Landau Level corresponding to the lowest energy Dirac cone near charge neutrality.

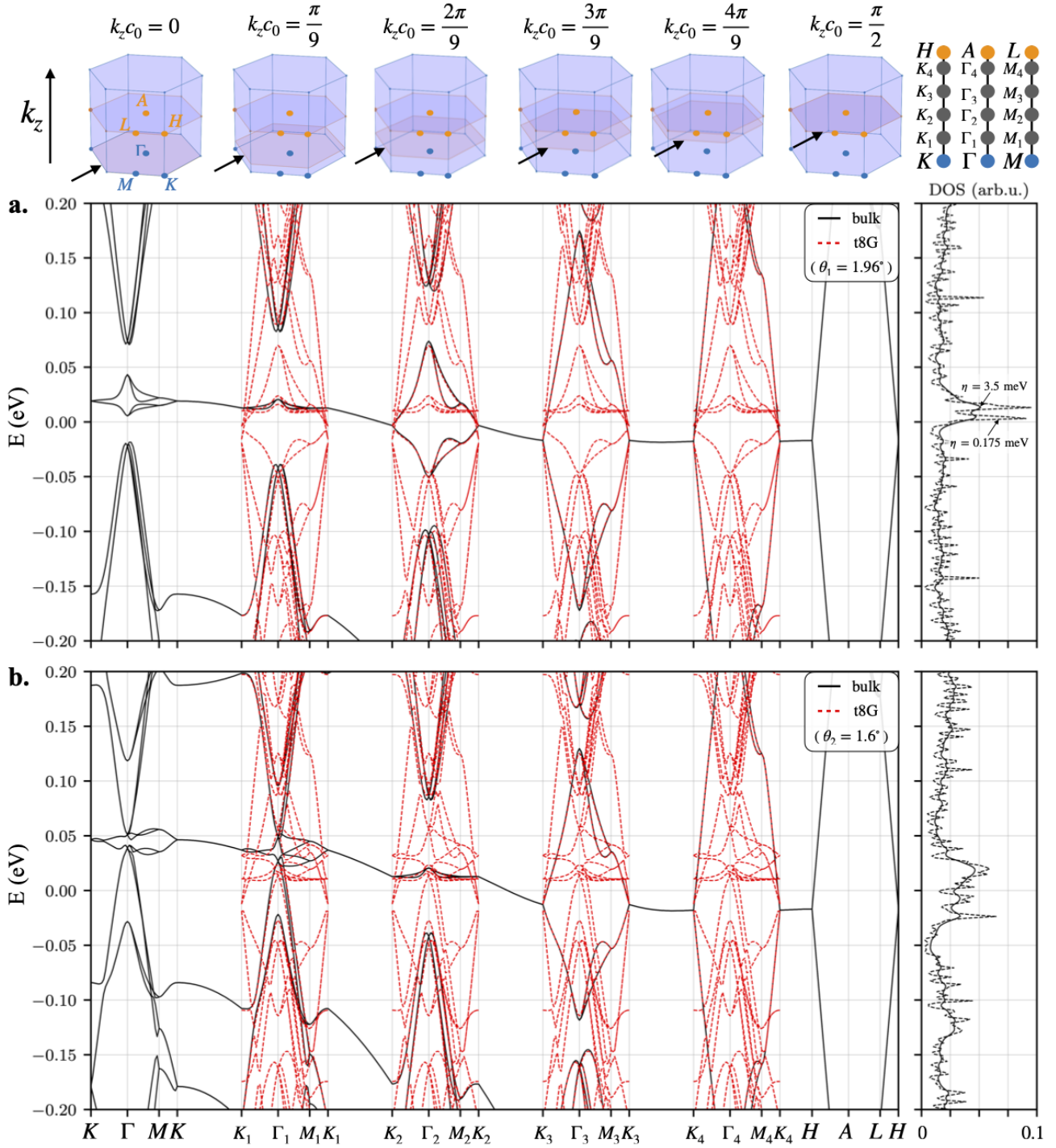


Figure 5. (color online) Comparison of bulk AT-graphite electronic bands in black at select $k_z c_0$ values given in Eq. (25) corresponding to $[K_i, \Gamma_i, M_i, K_i]$ planes against lattice relaxed t8G bands in red. Top **a.** and bottom **b.** panels represent two effective twist angles $\theta_{\text{eff}} = 1.96^\circ$ and $\theta_{\text{eff}} = 1.6^\circ$ corresponding to the magic angle of the first and second layers and actual calculations were done in a commensurate cell with $\theta = 2.00^\circ$ using $S' = 0.912$ and 1.119 . The $[K, \Gamma, M, K]$, and $[H, A, L, H]$ planes corresponding to $k_z c_0 = 0, \pi/2$ can be mapped by a finite system for $N \rightarrow \infty$. In the bottom panel **b.**, we see that the second bilayer band of t8G becomes very flat in the $[K_2, \Gamma_2, M_2, K_2]$ plane. These panels corresponding to different effective angles illustrate the coexistence of a continuum of magic angles in the bulk geometry. We provide in the Appendix Fig. D3 a similar comparison based on continuum models without including lattice relaxations.

tunneling in Eq. (15) to be the same. To illustrate the t2G bands that exist within a tNG band structure in the Hamiltonian and the subsequent mapping to the AT-graphite we overlay in Fig. 5 the bands for $N = 8$ case on the AT-graphite bands at select k_z values obtained at $\pi/9$, $2\pi/9$, $3\pi/9$ and $4\pi/9 - k_z c_0$ cuts. In the first panel, we see a clear agreement between the bulk AT-graphite and the t8G bands for the first magic-angle of the first bilayer band where the bulk is corrugation-free by design and the free-standing finite system contains corrugation. In the second panel, we set the effective twist angle to $\theta_{\text{eff}} = 1.6^\circ$ by tuning the coupling strength S' to the first magic-angle of the second bilayer band at $k_z c_0 = 2\pi/9$ -plane in the bulk band structure. In both cases we observe a good agreement between the bulk and the t8G system where the difference stems mainly from the different relaxation profiles. We provide a similar bulk-finite mapping based on the continuum model in the Appendix in Fig. D3 showing an even closer agreement due to the absence of relaxations. Decoupling of the bands into effective bilayers with different Fermi velocities was illustrated for few layers tNG in Fig. 3 for $N = 3, 4, 5, 6$ and we further illustrate this in Fig. 6 for a t20G system at $\theta_{\text{eff}} = 2.02^\circ$ twist. We note that adding an electric field in t20G allows to resolve the Dirac cones of the associated effective bilayer bands and brings the higher energy conduction and valence bands closer to the charge neutral point.

4. Summary and conclusions

We have carried out the stacking dependent atomic structure calculations of tNG systems up to $N = 6$ layers and shown that the highly symmetric AA'AA'... stacked sliding configuration is energetically the most stable of all possible alternatives indicating that these will be favored when devices are prepared experimentally. In particular, we find that there are barrier-free sliding paths towards the energetically stable symmetric stacking configuration.

From an electronic structure perspective, the lattice relaxation leads to small reductions in the magic angle predictions compared to analytical or continuum model calculations with fixed interlayer coupling strengths. This behavior has been confirmed numerically from the $N = 3$ all the way up to the bulk AT-graphite configuration. We have explained this behavior based on the progressive reduction of the integrated interlayer tunneling ω from small to large N limit that is mainly due to the decrease of in-plane strains when the layers are twisted to have larger angles that in turn reduces the relative area of AB/BA stacking regions. The relaxed lattice geometries also lead to electron-hole asymmetry enhancement and isolation of the flat bands from the rest of the spectrum at the Γ -point in tNG systems.

When we introduce a perpendicular electric field, charge is relocated from the inner layers towards the outer layers and leads to decoupled N Dirac bands that acquire

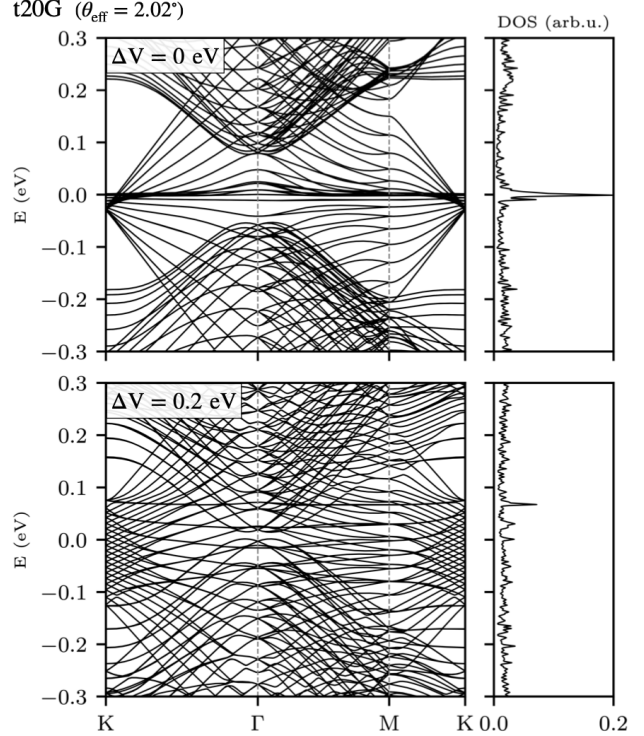


Figure 6. (color online) Electronic band structure and total DOS for a 20-layer twisted multilayer system for the effective first magic angle at $\theta_{\text{eff}} = 2.02^\circ$ corresponding to a minimal width at the Γ -point (equal to the $\theta = 2.02^\circ$ value based on the criterion of maximizing the DOS, for zero (top) and 0.2 eV top-bottom interlayer potential energy difference (bottom)). The interlayer potentials are modeled to linearly vary throughout the layers following Eq. (5). The physical commensurate angle and associated S' factor are summarized in Table B1. We can clearly resolve the 10 sets of bilayer systems and we notice that the electron and valence bands at the Γ -point overlap with the flat bands in presence of an electric field.

different Fermi velocity values. Only the $N = 4$ layered system leads to gap opening in the presence of an electric field near the first magic angle, while one or two Dirac cones survive near the charge neutral point in the case of $N = 5$ and $N = 6$ systems.

We have calculated the Landau levels in the quantum Hall regime for magnetic fields of up to $B = 50$ T. Except for the t3G case, we have shown that sufficiently strong perpendicular electric fields can deplete the density of states near charge neutrality for tNG systems leading to practically gapped phases.

Finally, we showed that the band structures in multilayer tNG can be mapped closely onto bulk AT-graphite bands at select k_z values following the decoupling of tNG bands into effective bilayer models where the interlayer tunneling values are proportional to the eigenenergies of a 1D-chain of layers, with small differences stemming from relaxation effects. The eigenvector amplitudes in each layer indicate the charge densities associated to the flat bands where the largest eigenvalue

eigenvectors tend to concentrate the charge at the middle layers while these redistribute towards the outer layers when we choose smaller twist angles.

Acknowledgement

N. L. was supported by the Korean National Research Foundation grant NRF-2020R1A2C3009142, Y. J. Park was supported by grant NRF-2021R1A6A3A13045898 and A. S. was supported by grant NRF-2020R1A5A1016518. J. A. was supported by the Korean Ministry of Land, Infrastructure and Transport (MOLIT) from the Innovative Talent Education Program for Smart Cities. J. J. was supported by the Samsung Science and Technology Foundation under project SSTF-BAA1802-06. We acknowledge computational support from KISTI through grant KSC-2021-CRE-0389, the resources of Urban Big data and AI Institute (UBAI) at the University of Seoul and the network support from KREONET.

- [1] Cao Y, Fatemi V, Demir A, Fang S, Tomarken S L, Luo J Y, Sanchez-Yamagishi J D, Watanabe K, Taniguchi T, Kaxiras E, Ashoori R C and Jarillo-Herrero P 2018 *Nature* **556** 80 ISSN 1476-4687
- [2] Park J M, Cao Y, Watanabe K, Taniguchi T and Jarillo-Herrero P 2021 *Nature* **590** 249–255 URL <https://doi.org/10.1038/s41586-021-03192-0>
- [3] Hao Z, Zimmerman A M, Ledwith P, Khalaf E, Najafabadi D H, Watanabe K, Taniguchi T, Vishwanath A and Kim P 2021 *Science* **371** 1133–1138 URL <https://doi.org/10.1126/science.abg0399>
- [4] Li X, Wu F and Das Sarma S 2020 *Phys. Rev. B* **101**(24) 245436 URL <https://link.aps.org/doi/10.1103/PhysRevB.101.245436>
- [5] Cea T, Walet N R and Guinea F 2019 *Nano Letters* **19** 8683–8689 URL <https://doi.org/10.1021/acs.nanolett.9b03335>
- [6] Wu F, Zhang R X and Das Sarma S 2020 *Phys. Rev. Research* **2**(2) 022010 URL <https://link.aps.org/doi/10.1103/PhysRevResearch.2.022010>
- [7] Moriyama S, Morita Y, Komatsu K, Endo K, Iwasaki T, Nakaharai S, Noguchi Y, Wakayama Y, Watanabe E, Tsuya D, Watanabe K and Taniguchi T 2019 Observation of superconductivity in bilayer graphene/hexagonal boron nitride superlattices (*Preprint arXiv:1901.09356*)
- [8] Liu X, Hao Z, Khalaf E, Lee J Y, Ronen Y, Yoo H, Najafabadi D H, Watanabe K, Taniguchi T, Vishwanath A and Kim P 2020 *Nature* **583** 221–225 URL <https://doi.org/10.1038/s41586-020-2458-7>
- [9] Nguyen V H, Hoang T X and Charlier J C 2022 Electronic properties of twisted multilayer graphene (*Preprint arXiv:2203.09188*)
- [10] Park J M, Cao Y, Watanabe K, Taniguchi T and Jarillo-Herrero P 2021 *Nature* **590** 249–255 URL <https://doi.org/10.1038/s41586-021-03192-0>
- [11] Park J M, Cao Y, Xia L, Sun S, Watanabe K, Taniguchi T and Jarillo-Herrero P 2021 *arXiv:2112.10760*
- [12] Leconte N, Jung J, Lebègue S and Gould T 2017 *Phys. Rev. B* **96**(19) 195431 URL <https://link.aps.org/doi/10.1103/PhysRevB.96.195431>
- [13] Bistrizter R and MacDonald A H 2011 *Proceedings of the National Academy of Sciences* **108** 12233–12237 URL <https://www.pnas.org/doi/abs/10.1073/pnas.1108174108>
- [14] Chebrolu N R, Chittari B L and Jung J 2019 *Physical Review B* **99** 235417 ISSN 2469-9950
- [15] Trambly de Laissardière G and Mayou D 2013 *Phys. Rev. Lett.* **111**(14) 146601 URL <https://link.aps.org/doi/10.1103/PhysRevLett.111.146601>
- [16] Leconte N, Javvaji S, An J and Jung J 2019 Relaxation effects in twisted bilayer graphene: a multi-scale approach (*Preprint arXiv:1910.12805*)
- [17] Jung J, Raoux A, Qiao Z and MacDonald A H 2014 *Phys. Rev. B* **89**(20) 205414 URL <https://link.aps.org/doi/10.1103/PhysRevB.89.205414>
- [18] Jung J, Laksono E, DaSilva A M, MacDonald A H, Mucha-Kruczyński M and Adam S 2017 *Phys. Rev. B (Preprint)* **1706.06016**
- [19] McKinnon B and Choy T 1993 *Australian Journal of Physics* **46** 601 URL <https://doi.org/10.1071/ph930601>
- [20] Jung J and MacDonald A H 2013 *Physical Review B* **87** 195450 ISSN 1098-0121
- [21] Laissardière G T d, Mayou D and Magaud L 2012 *Physical Review B* **86** 125413 ISSN 1098-0121
- [22] Chittari B L, Leconte N, Javvaji S and Jung J 2018 *Electronic Structure* **1** 015001
- [23] Khalaf E, Kruchkov A J, Tarnopolsky G and Vishwanath A 2019 *Phys. Rev. B* **100**(8) 085109 URL <https://link.aps.org/doi/10.1103/PhysRevB.100.085109>
- [24] Fan Z, Garcia J H, Cummings A W, Barrios-Vargas J E, Panhans M, Harju A, Ortmann F and Roche S 2021 *Physics Reports* **903** 1–69 ISSN 0370-1573 linear scaling quantum transport methodologies URL <https://www.sciencedirect.com/science/article/pii/S0370157320304245>
- [25] Cresti A 2021 *Phys. Rev. B* **103**(4) 045402 URL <https://link.aps.org/doi/10.1103/PhysRevB.103.045402>
- [26] Brenner D W, Shenderova O A, Harrison J A, Stuart S J, Ni B and Sinnott S B 2002 *Journal of Physics: Condensed Matter* **14** 783–802 URL <https://doi.org/10.1088/0953-8984/14/4/312>
- [27] Wen M, Carr S, Fang S, Kaxiras E and Tadmor E B 2018 *Phys. Rev. B* **98**(23) 235404 URL <https://link.aps.org/doi/10.1103/PhysRevB.98.235404>
- [28] Plimpton S 1995 *Journal of Computational Physics* **117** 1–19 URL <https://doi.org/10.1006/jcph.1995.1039>
- [29] Bitzek E, Koskinen P, Gähler F, Moseler M and Gumbusch P 2006 *Phys. Rev. Lett.* **97**(17) 170201 URL <https://link.aps.org/doi/10.1103/PhysRevLett.97.170201>
- [30] Rowe P, Deringer V L, Gasparotto P, Csányi G and Michaelides A 2020 *The Journal of Chemical Physics* **153** 034702 URL <https://doi.org/10.1063/5.0005084>
- [31] Carr S, Li C, Zhu Z, Kaxiras E, Sachdev S and Kruchkov A 2020 *Nano Letters* **20** 3030–3038 URL <https://doi.org/10.1021/acs.nanolett.9b04979>
- [32] Ledwith P J, Khalaf E, Zhu Z, Carr S, Kaxiras E and Vishwanath A 2021 *arXiv:2111.11060*
- [33] Nam N T and Koshino M 2017 *Physical Review B* **96** 075311 ISSN 2469-9950
- [34] Koshino M and Ando T 2008 *Phys. Rev. B* **77**(11) 115313 URL <https://link.aps.org/doi/10.1103/PhysRevB.77.115313>
- [35] Stauber T, Low T and Gómez-Santos G 2018 *Phys. Rev. Lett.* **120**(4) 046801 URL <https://link.aps.org/doi/10.1103/PhysRevLett.120.046801>
- [36] Kim C J, Sánchez-Castillo A, Ziegler Z, Ogawa Y, Noguez C and Park J 2016 *Nature Nanotechnology* **11** 520–524 URL <https://doi.org/10.1038/nnano.2016.3>

Appendix A. Potential and elastic energy maps

In Fig. A1, we provide the potential energy and elastic energy contributions for the t3G and t4G systems. We separate these from our LAMMPS calculation by summing separately the pair-wise interactions between inter-layer atoms (potential energy) and intra-layer atoms (elastic energy). We map out the profiles using the elastic and potential energy

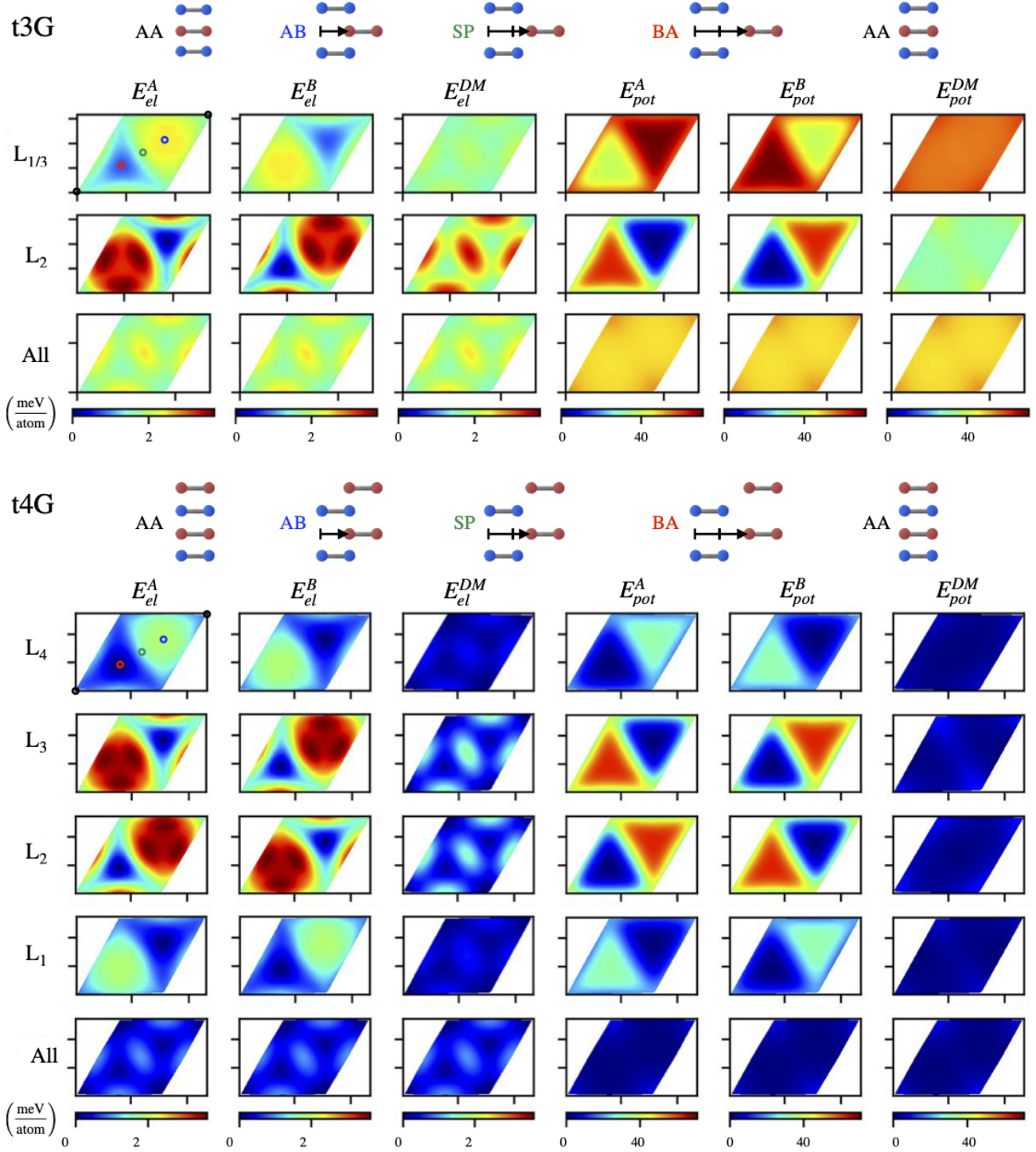


Figure A1. Layer-, sublattice-, and dimer (DM)-resolved maps of local elastic (E_{el}) energy in Eq. (A.1) and potential (E_{pot}) energy in Eq. A.2 for the minimum energy sliding t3G and t4G configurations are shown in the top and bottom panels respectively. Because the outer layers have only one interface the elastic and potential energy variations are roughly half of the inner layers that have two. We separate both the sublattice A and B contributions as well as the L_1 (equal to L_3) and L_2 layer contributions. DM refers to the dimer contribution which is the average of A and B sublattice contributions and All is the average of all the different layer contributions. The energies in the figure are given in meV/atom. We apply a constant energy shift for both systems of -7.397 eV/atom for the elastic energies and 0.079 eV/atom for the potential energies to ease visual comparison between the different panels. This brings to zero the smallest elastic or potential energy value shown in the graphs. We notice that the outer layers carry about half of the potential and elastic energy differences due to the single interface when compared with the middle layer(s) that have two. The average of all layer contributions fluctuate around a constant average value by a relatively small amount with respect to variations in an individual layer. The potential energy contributions are greater in magnitude than the elastic energies and lead energetically favorable (AB/BA) and unfavorable regions (AA). The average elastic energy is highest at the SP regions. Distinct layer/sublattice dependent elastic and potential energies reflect the chirality of the alternating twist angle signs.

contributions from each atom i calculated as

$$E_i^{\text{el}} = \sum_{j \in \text{layer } i} \phi_{ij} \quad (\text{A.1})$$

$$E_i^{\text{pot}} = \sum_{j \in \text{layer } i} \phi_{ij} = \sum_{j \in \text{any layer}} \phi_{ij} - E_i^{\text{el}} \quad (\text{A.2})$$

where ϕ_{ij} are the pair-wise interactions between atoms i and j modeled by the DRIP potential [27] for interlayer interactions and the REBO2 potential [26] for intralayer interactions. The maps of the outer layers show a factor $\sim 1/2$ in terms of the potential energy differences due to having only one interface with another layer. As mentioned in the main text, based on the potential energy, the AA stacking shows the highest binding energy, or conversely the lowest free energy; the energetically favorable and unfavorable regions can thus be fully inferred from the potential energy maps. This stands in contrast with the layer resolved potential energy maps where AA-stacking corners do not appear as the energetically least favorable. In terms of the elastic energy, we observe that, when adding up all layers, the strongest strain is located at the center of the SP regions with the symmetry stacking AA and AB positions being the ones containing the least amount of elastic strain. We further note that, due to the alternating rotation directions between consecutive layers, the layer and sublattice-resolved energy maps show alternating chirality both for their elastic and potential contributions. The chiral nature of t2G has been linked to strong optical activity at finite frequencies corresponding to transitions around the M point [35, 36]. The matching trends for t3G and t4G suggest that similar conclusions can be drawn for increasing number of layers.

Appendix B. Magic angle extraction and fine DOS features

In Fig. 2, we plotted the numerical predictions of the magic angles based on DOS calculations to avoid the numerical complications of having to use relatively small commensurate cells for electronic band structure calculations. Using Lanczos recursion, we are able to finely scan additional angles around the analytical predictions, here done in steps of approximately $\Delta\theta \sim 0.005^\circ$. We then considered two different regimes for the extraction of the flattest band, *i.e.* the largest peak in the DOS, based on the broadening value η in Eq. (21). In Fig. B1, we first consider a relatively large broadening of about $\eta = 3.5$ meV which has the tendency peak at one single value in the DOS. For this regime, we thus report the magic angle as the angle corresponding to this largest DOS value. Then, we also consider a second regime using a numerical broadening of $\eta = 0.175$ meV which allows to resolve all the fine electronic band structure features, similar to what had been reported in Ref. [16] for tBG. Under these conditions, we observe a large number of peaks in the DOS, hence we extract the range of magic angles reported in Fig. 2 for smallest broadening

to be the one encompassed by the angles corresponding to the outer peaks in the illustrated range with an amplitude above a certain arbitrary threshold. Orange lines indicate these values. We note that unlike for the finite systems, the global peak of the DOS maxima for the bulk seems to be mostly insensitive to the chosen broadening due to the large number of bands contributing concurrently to the broad DOS shown in the side panels of Fig. 5. To illustrate how these fine features match with specific bands in the electronic band structure and are not rooted in numerical noise, we focus on the t3G system in Fig. B2. Here we have used the commensurate cell at $\theta = 1.538^\circ$ to calculate all the curves, changing the value of S' and finding the corresponding effective angle using Eq. (18). We use exact diagonalization for both the electronic bandstructure and the DOS here with a broadening of $\eta = 0.1$ meV. Unlike for the larger broadening value used in the main text, the striking observation here is that using a small broadening value of $\eta = 0.1$ meV the flattest band as predicted by the minimum in bandwidth at Γ , corresponding to an effective magic angle of $\theta_{\text{eff}} = 1.51^\circ$ is different from the flattest as predicted by the maximum in DOS, namely $\theta_{\text{eff}} = 1.56^\circ$. We can relate this angle with the largest DOS peak to the very flat valence band. These observations on the t3G system suggests that for the other tNG systems the double or triple peak configuration developing for the smallest broadening probably also corresponds to valence and conduction bands reaching maximum flatness at different angles. We note that this effective angle procedure for small commensurate cells used here in Fig. B2 is the same one we used for the band structure calculations in the main text. We summarize in Table B1 these different system-specific parameters for the band structures in the main text and provide for reference also the θ -values as predicted by the maximum in DOS observing that the magic angles using either criterion are very similar for the finite systems.

Appendix C. Impact of relaxation effects on magic angle predictions and higher-order magic angles

In the main text, we elucidated how the in-plane strain plays an important role in explaining the decrease in magic angle observed when compared with the analytical predictions based on the t2G hopping values. Here we provide some additional figures and discussions to go into more detail on these considerations. In Fig. C1, we show how the bulk equilibrium interlayer distance varies with twist angle and how it compares with the average interlayer distance of a t2G system. We notice that this bulk value can almost exactly be predicted using the ratios of AA, AB/BA and SP-stacking present at a specific rotation angle, where we use the conventions outlined in Ref. [16] to assign a stacking label to each atom, following

$$\bar{c}_{ij}^{\text{bulk}} = r_{\text{AA}} c_0^{\text{AA}} + r_{\text{AB/BA}} c_0^{\text{AB/BA}} + r_{\text{SP}} c_0^{\text{SP}} \quad (\text{C.1})$$

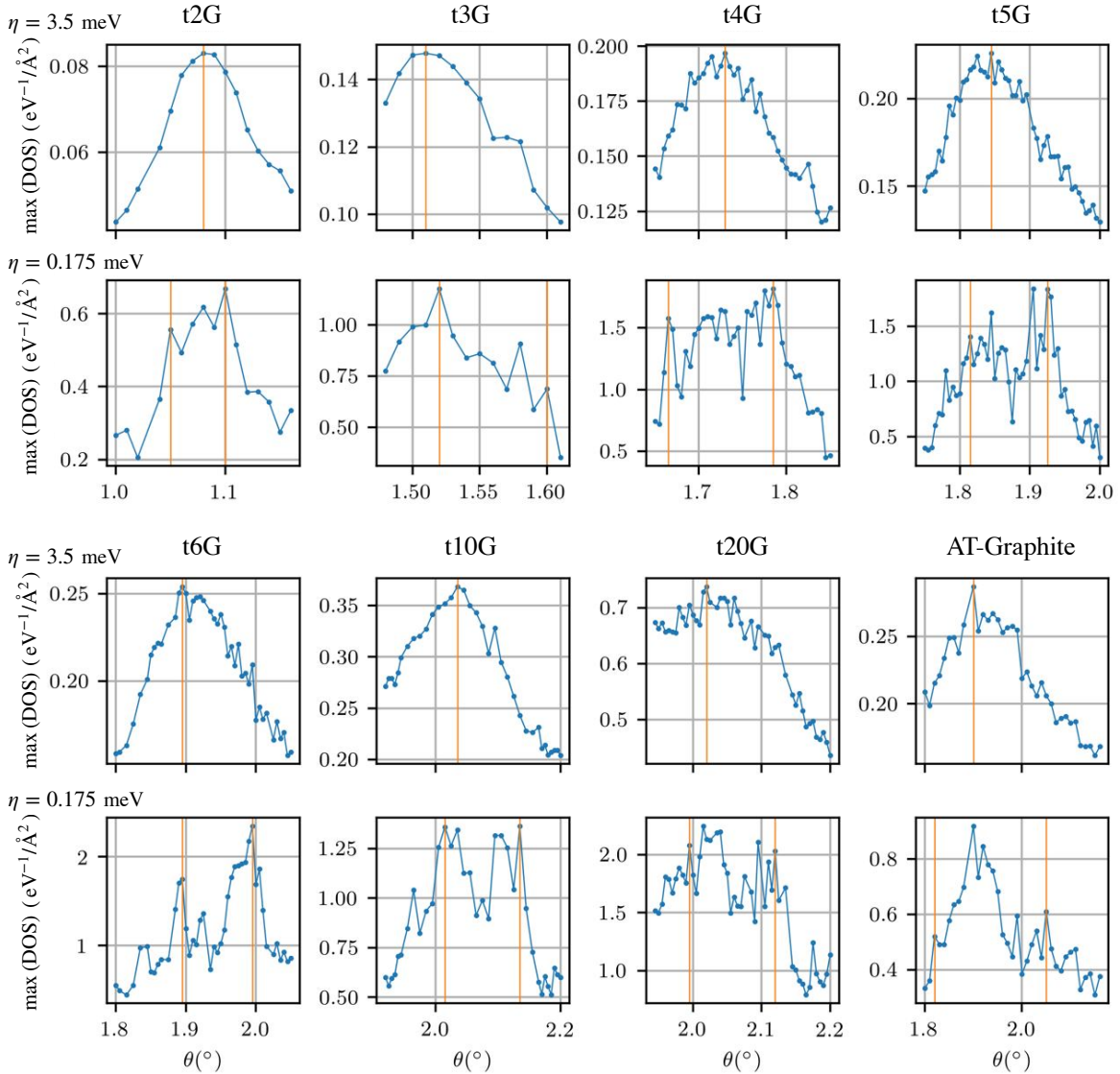


Figure B1. (color online) Using a broadening η of about (i) 3.5 and (ii) 0.175 meV in Eq. (21), we extract the magic angles to be (i) the ones corresponding here to the highest value in the range plotted here where $\max(\text{DOS})$ is the maximum of the DOS curve for a specific angle in a range close to the Fermi energy where the flat band is expected to be and (ii) the ones corresponding to the angles encompassed by the outer $\max(\text{DOS})$ peaks that have an amplitude above an arbitrary threshold within the range plotted here. These values are then reported in Fig. 2 and indicated here by orange lines. The finite resolution of angle points as well as the partially arbitrary choice in what is considered to be a peak causes some uncertainty in the extraction of these magic angles. We note that for simplicity the angle-sweep for the AT-Graphite system are done for a fixed interlayer distance of 3.328 Å, although a small angle-dependence of this distance is observed as illustrated in Fig. C1. This simplification should affect the magic angle extraction by 0.02° at most.

where r_X corresponds to the ratio of atoms in X -stacking with respect to the total number of atoms, while c_X is the equilibrium interlayer distance for stacking X , equal to 3.313, 3.402 and 3.317 Å for AB/BA, AA and SP-stacking, respectively. The free-standing system shows slightly larger values than the bulk since it is not constrained by the periodic boundaries in the vertical direction. In Fig. C2, we look at the average interlayer distance for both freestanding tNG systems as well as their counterparts fixing the outer-layer atoms. We notice that the low- N tNG systems show a larger average interlayer distance than the high- N systems which

can be rationalized by the fact that these systems contain in relative terms more single-interface layers where the in-plane relaxation is reduced by almost a factor 2 compared to the inner layers that have two interfaces. This reduction of in-plane relaxation reduces the lattice reconstruction effects and in turn increases the average interlayer distance due to a higher proportion of AA-stacking entering Eq. (C.1).

In order to check if the relaxation effects that tend to decrease the analytical predictions also impact the higher-order magic angles, namely the smaller magic angles corresponding to the effective bilayers with smaller

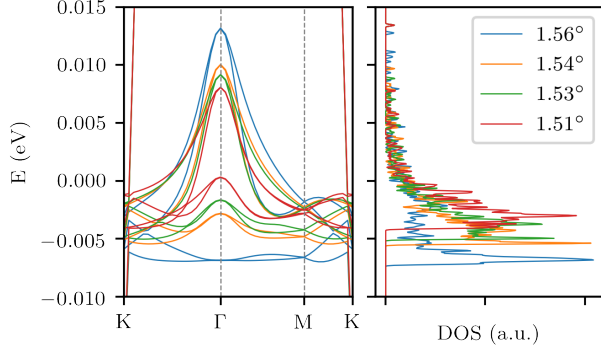


Figure B2. (color online) For t3G, we can see the close agreement between the bandstructures and DOS calculations where different maxima are observed depending on which of the flat bands is flatter for a specific angle. The values of S' used in this figure, related to θ_{eff} using Eq. (18), are 0.880, 0.895, 0.900 and 0.914, respectively. For the very small broadening of $\eta = 0.1$ meV used here, the $\theta = 1.56^\circ$ system corresponding to the largest DOS is different from the magic angle of 1.51° based on the minimal bandwidth of the flat bands at the Γ -point.

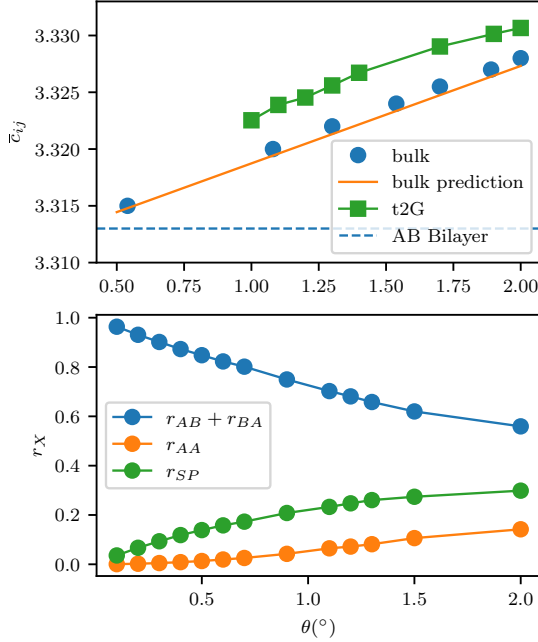


Figure C1. (color online) *Top panel:* Angle-dependent average interlayer distance \bar{c}_{ij} for the twisted bulk configuration and the free-standing t2G systems. The orange line uses Eq. (C.1) to predict the equilibrium bulk interlayer distance using the AA, AB/BA and SP-stacking ratios and their respective equilibrium interlayer distance. We add the equilibrium distance for AB-stacked graphene for reference using the blue-dashed line. *Bottom panel:* The numerical data representing the stacking area ratio r_X from Eq. (C.1) based on free-standing bilayer calculations and used in the top panel for the bulk system based on the stacking-assignment conventions from Ref. [16]. These ratios add up to 1 where the moire maps of the smallest angles are almost exclusively formed by the most stable AB and BA stacking regions.

N	θ_{cell}	θ	θ_{eff}	S'	$i j$	# Atoms
2	1.08	1.08	1.08	0.895	31 30	11164
3	1.54	1.51	1.51	0.914	21 20	8322
4	1.79	1.73	1.72	0.932	19 18	8216
5	1.89	1.82	1.84	0.921	18 17	9190
6	2.00	1.89	1.90	0.940	17 16	9804
10	2.00	2.01	2.03	0.881	17 16	16340
20	2.00	2.02	2.02	0.884	17 16	32680
bulk $_{\theta_1}$	2.00	1.90	1.96	0.912	17 16	3268
bulk $_{\theta_2}$	2.00	NA	1.6	1.119	17 16	3268

Table B1. System-specific parameters where θ is the experimentally most relevant magic angle predicted by our DOS calculations on very large commensurate cells using Eq. (21) while θ_{cell} are the commensuration cells that were used to perform the band structure calculations using the modified S' values to capture the flattest bands using the criterion that minimizes the bandwidth of the flat bands at the Γ -point. The resulting angles that are probed based on this criterion are given by θ_{eff} and give almost the same angle values as the θ ones coming from the maximum of the DOS. The two S' values for the bulk correspond to the two panels from the bulk bandstructure figure, *i.e.* the angles corresponding to the minimization of the first magic angle bandwidth at the Γ_1 (Γ_2) points for the first (second) bilayer bands, respectively. θ_2 based on the maximum of DOS is not available (NA) due to being hard to resolve among the many other states present in the bulk.

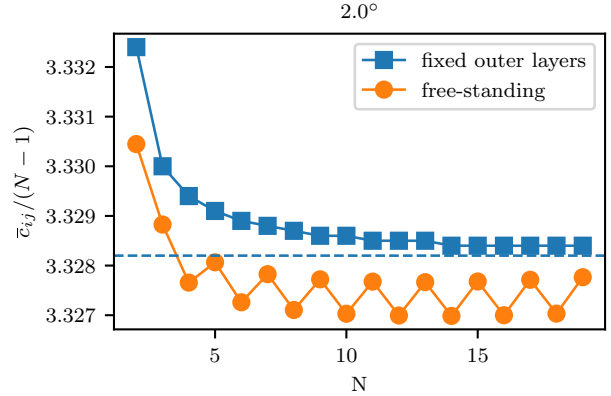


Figure C2. (color online) Layer-dependent average interlayer distance normalized by the number of layers for a 2° twisted system where we allow for out-of-plane corrugation (orange) and where we preclude this corrugation by fixing the z-coordinate of the outer layers (blue). The free-standing system reaches a minimum around $N=14$ thus giving a possible reason for the maximum in magic angle at $N = 10$ observed in Fig. 2 due to increased tunneling and thus larger magic angle. When fixing the outer-layers, we observe that near-bulk behavior is reached after 5 layers where the interlayer distance departs by 0.001 \AA from the bulk-value for this angle.

interlayer tunneling, we perform similar DOS calculations on the first magic angle of the second bilayer bands of t4G, t5G and t6G. We obtain values that are very similar to the analytical predictions reported in Table D2. This stands in contrast with our previous conclusions on the first magic angle of the first bilayer bands stating that the

magic angles are reduced due to relaxation effects. By calculating the layer-resolved DOS we observe that the states associated to the flat bands from the second bilayer bands are located preferentially away from the central layers of the system, including a partial occupation on the outer-most layers. These outer-layer carry a smaller amount of in-plane relaxation due to interfacing only with one other layer, hence the expected magic angle reduction is less pronounced.

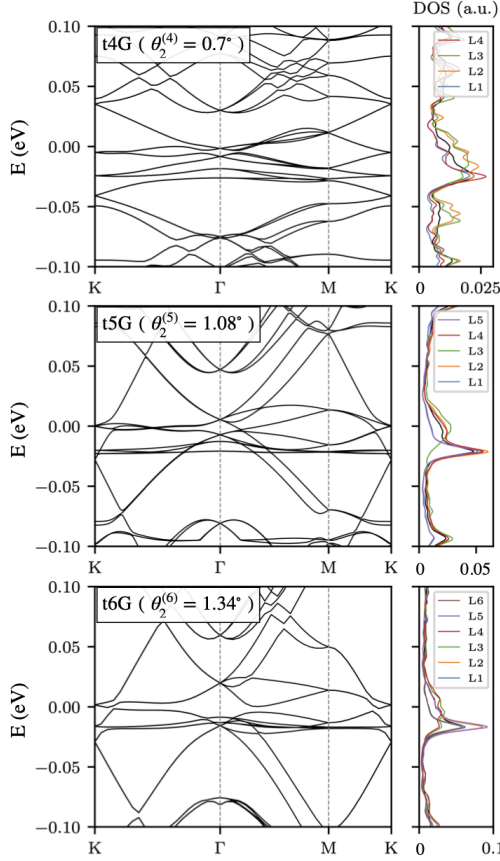


Figure C3. (color online) Second magic angle for t4G, t5G and t6G at $\theta = 0.7, 1.08$ and 1.34° , respectively, based on the maximum in the DOS criterion. The lowest flat band corresponds to the second bilayer band while the the highest nearly flat band comes from the first bilayer band. The DOS is calculated using a broadening of $\eta = 3.5$ meV. Our predictions agree with the analytical predictions in absence of relaxation effects suggesting the latter are less important for these bands than for the first magic angle from the first bilayer bands. This can be rationalized by the fact the states associated with these bands are pushed away from the most inner-layer bands, as illustrated by the layer-resolved DOS, where relaxation effects are weaker. The amplitude of the total density of states in black is divided by the number of layers for comparison purposes.

Appendix D. From tNG to decoupled $t2G$ s

The continuum model Hamiltonian \mathcal{H}_k of Eq. (1) can be decoupled the series of decoupled $t2G$ -like Hamiltonian [23] based on singular value decomposition of a layer hopping matrix where odd and even layers were separated. Here we

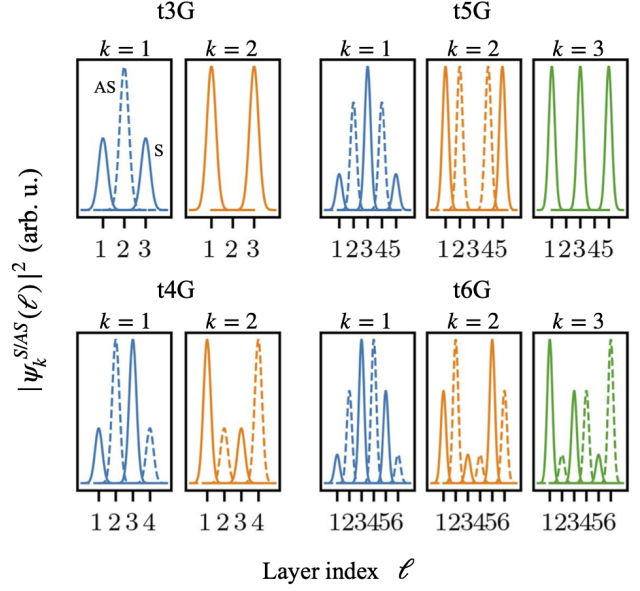


Figure D1. (color online) Probability distribution of the two wavefunctions with the symmetric(S) and anti-symmetric(AS) combinations of the two states based on the eigenstates with opposite sign eigenvalues $\lambda_k = -\lambda_{N+1-k}$ in Eq. (15). The states with $k = 1$, corresponding to the first magic angle of the first bilayer band in this mapping procedure, are preferentially located on the inner layer(s) while the states next in order with $k = 2$, corresponding to the first magic angle of the second bilayer band, get redistributed away from the inner layers where relaxation effects and associated angle reduction effects are weaker when compared to the analytically predicted values based on a constant t2G value.

show that equivalent results can be obtained by applying in twisted systems the same basis change and alternating layer/sublattice grouping scheme outlined in Ref. [34] for zero twist Bernal stacked graphene multilayers.

To easily decouple the states, we first rearrange the order of the basis $\{|A_\ell\rangle, |B_\ell\rangle\}$ for $\ell = 1, 2, \dots, N$ through the transformation matrix P from $(\psi_{A_1}, \psi_{B_1}, \psi_{A_2}, \psi_{B_2}, \dots, \psi_{A_N}, \psi_{B_N})^T$ to $(\psi_A^o, \psi_B^o, \psi_A^e, \psi_B^e)^T$ where $\psi_s^o = (\psi_{s_1}, \psi_{s_3}, \dots, \psi_{s_{2N_o-1}})^T$ and $\psi_s^e = (\psi_{s_2}, \psi_{s_4}, \dots, \psi_{s_{2N_e}})^T$ for the sublattice $s = A, B$ and the number of odd/even layers N_o/e . The transformed Hamiltonian from that in Eq. (1) is

$$P^\dagger \mathcal{H}_k P = \begin{pmatrix} h_{oo}^{AA} \mathbf{1}_o & h_{oo}^{AB} \mathbf{1}_o & T_{oe}^{AA} \mathbf{C}_1 & T_{oe}^{AB} \mathbf{C}_1 \\ h_{oo}^{BA} \mathbf{1}_o & h_{oo}^{BB} \mathbf{1}_o & T_{eo}^{BA} \mathbf{C}_1 & T_{eo}^{BB} \mathbf{C}_1 \\ T_{eo}^{AA} \mathbf{C}_1^\dagger & T_{eo}^{AB} \mathbf{C}_1^\dagger & h_{ee}^{AA} \mathbf{1}_e & h_{ee}^{AB} \mathbf{1}_e \\ T_{eo}^{BA} \mathbf{C}_1^\dagger & T_{eo}^{BB} \mathbf{C}_1^\dagger & h_{ee}^{BA} \mathbf{1}_e & h_{ee}^{BB} \mathbf{1}_e \end{pmatrix} \quad (\text{D.1})$$

where $\mathbf{1}_{o/e} = \sum_{n=1}^{N_{o/e}} \delta_{n,n}$ are the identity matrices and $\mathbf{C}_1 = \sum_{i=1}^{N_o} [\delta_{n,n} + \delta_{n+1,n}]$ reflects $N_o \times N_e$ inter-layer tunneling matrices between the odd and even layers, and $P = \sum_{n=1}^{N_o} (\delta_{2(2n-1)-1, n} + \delta_{2(2n-1), n+N_o}) + \sum_{n=1}^{N_e} (\delta_{2(2n), n+2N_o} + \delta_{2(2n), n+2N_o+N_e})$ is the transformation matrix. For simplicity, we assume zero on-site energy for each layer denoting $h_{oo}^{AA/BB} = h_{ee}^{AA/BB} = 0$. The k vector dependence is only included in $h_{oo}^{AB} e^{i\theta/2} = [h_{oo}^{BA} e^{-i\theta/2}]^\dagger =$

$\hbar v_F \pi_k^\dagger$ and $h_{ee}^{AB} e^{-i\theta/2} = [h_{ee}^{BA} e^{+i\theta/2}]^\dagger = \hbar v_F \pi_{k'}^\dagger$. Interlayer tunneling matrices $T_{oe}^{\alpha\beta}(\mathbf{r}) = T_{eo}^{\alpha\beta}(-\mathbf{r}) = \sum_{j=0,\pm} T_j^{\alpha\beta}(\mathbf{r})$ are the same as in Eq. (3) where

$$\begin{aligned} & \left(T_j^{AA}(\mathbf{r}), T_j^{AB}(\mathbf{r}), T_j^{BA}(\mathbf{r}), T_j^{BB}(\mathbf{r}) \right)^T \\ &= e^{-i\mathbf{Q}_j \cdot \mathbf{r}} (\omega', \omega e^{-i\phi_j}, \omega e^{+i\phi_j}, \omega')^T. \end{aligned}$$

Noting that \mathbf{C}_1 resembles the off-diagonal parts of the 1-dimensional chain system and they can easily be decoupled by even and odd atoms, we adopt the new sublattice $s = A, B$ resolved basis $\left\{ |\tilde{\psi}_k^{\text{odd}(A)}\rangle, |\tilde{\psi}_k^{\text{odd}(B)}\rangle, |\tilde{\psi}_k^{\text{even}(A)}\rangle, |\tilde{\psi}_k^{\text{even}(B)}\rangle \right\}$ as in Eq. (22) where

$$|\tilde{\psi}_k^{\text{odd}(s)}\rangle = \sum_{\ell=1}^N \psi_k^S(\ell) |s\ell\rangle, \quad |\tilde{\psi}_k^{\text{even}(s)}\rangle = \sum_{\ell=1}^N \psi_k^{AS}(\ell) |s\ell\rangle \quad (\text{D.2})$$

with the symmetric(S)/anti-symmetric(AS) combinations of two wave functions for each layer defined as

$$\psi_k^S(\ell) = \frac{\psi_k(\ell) + \psi_{N+1-k}(\ell)}{\sqrt{2}} = \sqrt{2} (-1)^{(\ell-1)} \psi_k(\ell) \quad (\text{for odd } \ell)$$

$$\psi_k^{AS}(\ell) = \frac{\psi_k(\ell) - \psi_{N+1-k}(\ell)}{\sqrt{2}} = \sqrt{2} (-1)^{(\ell-1)} \psi_k(\ell) \quad (\text{for even } \ell) \quad (\text{D.3})$$

with $k = 1, 2, \dots, N_e$ following Eq. (15)–(22) in the main text.

The final decoupled Hamiltonian is

$$\tilde{\mathcal{H}}_k = \tilde{P}^\dagger P^\dagger \mathcal{H}_k P \tilde{P} = \begin{pmatrix} h_{oo}^{AA} \mathbf{1}_o & h_{oo}^{AB} \mathbf{1}_o & T_{oe}^{AA} \Lambda & T_{oe}^{AB} \Lambda \\ h_{oo}^{BA} \mathbf{1}_o & h_{oo}^{BB} \mathbf{1}_o & T_{oe}^{BA} \Lambda & T_{oe}^{BB} \Lambda \\ T_{eo}^{AA} \Lambda & T_{eo}^{AB} \Lambda & h_{ee}^{AA} \mathbf{1}_e & h_{ee}^{AB} \mathbf{1}_e \\ T_{eo}^{BA} \Lambda & T_{eo}^{BB} \Lambda & h_{ee}^{BA} \mathbf{1}_e & h_{ee}^{BB} \mathbf{1}_e \end{pmatrix} \quad (\text{D.4})$$

that becomes the series of decoupled t2G-like Hamiltonian

$$\begin{aligned} \mathcal{H}_k^{(\text{dec})} &= P \tilde{\mathcal{H}}_k P^\dagger \\ &= \mathcal{H}_{k\lambda_1}^{(t2G)} \oplus \mathcal{H}_{k\lambda_2}^{(t2G)} \oplus \dots \oplus \mathcal{H}_{k\lambda_{N_e}}^{(t2G)} \\ &\quad \left(\oplus \mathcal{H}_k^{(1G)} \right) \end{aligned} \quad (\text{D.5})$$

where $\Lambda = \sum_k \lambda_k \delta_{k,n}$ is the diagonal $N_o \times N_e$ matrices with $k, n = 1, 2, \dots, N_e$ with the eigen value λ_k of 1d chain in Eq. (15). The transform matrix $\tilde{P} = \text{diag}(\tilde{P}_o, \tilde{P}_o, \tilde{P}_e, \tilde{P}_e)$ consists of $[\tilde{P}_{o/e}]_{n,k} = \psi_k^{S/AS}(\ell)$ with $k, n = 1, 2, \dots, N_{o/e}$, $\ell = 2n$ for even atoms, and $\ell = 2n - 1$ for odd atoms.

We can write the k -th decoupled t2G eigen functions satisfying $\mathcal{H}_k^{(\text{dec})}(\mathbf{r}) \Psi_{\lambda_k}^{t2G}(\mathbf{r}) = \Lambda_{\lambda_k}(\mathbf{r}) \Psi_{\lambda_k}^{t2G}(\mathbf{r})$ in terms of

the linear combination of the states for each layer,

$$\begin{aligned} \Psi_{\lambda_k}^{t2G}(\mathbf{r}) &= \sum_{\ell=1}^N [\tilde{P}_{o/e}]_{n,k} \left[\sum_{s=A,B} \Psi_{\lambda_k}^{(s\ell)}(\mathbf{r}) \right] \\ &= \sum_{\ell=1}^N \left[\sqrt{2} (-1)^{(\ell-1)} \sqrt{\frac{2}{N+1}} \sin(\kappa_k \ell) \right] \Psi_{\lambda_k}^{(\ell)}(\mathbf{r}), \end{aligned} \quad (\text{D.6})$$

for $k = 1, 2, \dots, N_e$.

In order to understand the spatial distribution of states as shown the far-most right panels in Fig. 3, we use this decoupling procedure to confirm in Fig. D1 that the highest eigenenergies with value $k = 1$ in Eq. (15) shows the same distribution of states as the first magic angle shown from Fig. 3 and the states with index $k = 2$ match the distribution of states from the layer-resolved DOS at the energy from the second magic angle in Fig. C3.

We further provide numerical confirmation of the decoupling procedure by illustrating how the scaling factor λ_k from Eq. 15 allows the first magic angle of tNG to coincide with the first magic angle of t2G. This is illustrated in Fig. D2 for λ_1 and λ_2 . This figure illustrates that the analytical predictions are quite accurate using the continuum model but based on the observations drawn from Fig. 2 we expect a departure from this ideal trend when realistic strain profiles are included. Table D1 summarizes the first magic

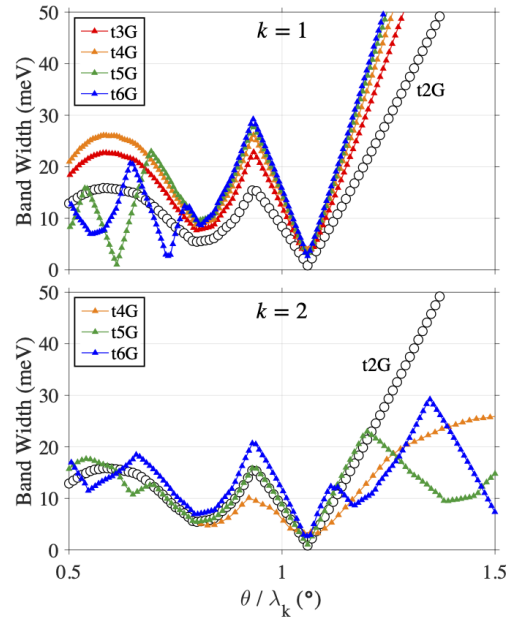


Figure D2. (color online) Band width profile of t2G~t6G calculated by a continuum model as a function of twist angle θ . The magic angle of tNG at which the band widths are minimized coincides with the first magic angle of t2G with the factor $\lambda_k = 2 \cos\left(\frac{\pi k}{N+1}\right)$ in Eq. (15).

angles for t2G all the way to the bulk obtained numerically using the continuum model, while Table D2 provides the θ_i values corresponding to the so called chiral model's α_i

values from Ref. [23] taking as t2G reference the value of $\theta_1^{(2)} = 1.08^\circ$.

N	$\theta_1^{(N)}$	N	$\theta_1^{(N)}$
2	1.06	8	2.00
3	1.50		1.62
4	1.71		1.06
	0.67	10	2.03
5	1.84		1.78
	1.06		1.39
6	1.91		0.88
	1.32	20	2.10
	0.47	bulk	2.12

Table D1. The magic angles for tNG numerically obtained by a continuum model with constant $\omega = 0.12$ eV, and $\omega' = 0.0939$ eV.

N	$\theta_1^{(N)}$	$\theta_2^{(N)}$	$\theta_3^{(N)}$	$\theta_4^{(N)}$	$\theta_5^{(N)}$	$\theta_6^{(N)}$
2	1.080	0.285	0.169	0.120	0.093	0.076
3	1.528	0.246	0.239	0.170	0.132	0.108
4	1.748	0.461	0.273	0.194	0.151	0.123
	0.668	0.176	0.104	0.074	0.058	0.047
5	1.872	0.494	0.292	0.208	0.161	0.132
	1.080	0.285	0.169	0.120	0.093	0.076
6	1.947	0.513	0.304	0.216	0.168	0.137
	1.346	0.355	0.210	0.150	0.116	0.095
	0.480	0.127	0.075	0.053	0.041	0.034

Table D2. Magic angle families $\theta_1^{(N)} \sim \theta_6^{(N)}$ in the chiral limit ($\omega' = 0$) can be converted from the $\alpha_1 \sim \alpha_6$ values from Ref. [23] using Eq. (14) with $v_F = (\sqrt{3}a/2\hbar)|t_0| \approx 1 \times 10^6$ m/s with a nearest hopping parameter $t_0 = -3.1$ eV, the intersublattice interlayer coupling $\omega_{AB'} = 0.1242$ eV, and $k_D = 4\pi/3a$ with a lattice constant $a = 2.46$ Å.

We finally illustrate in Fig. D3 a similar finite-to-bulk bandstructure calculation as in Fig. 5, but using the continuum model. We observe perfect overlap at the selected cuts for the bulk with the corresponding t8G bilayer bands as the relaxation profiles are exactly the same by design when using the continuum model.

tNG bulk ($\theta^{\text{bulk}} = \theta_k^{(8)}$, $\omega = 0.12$ eV, $\omega' = 0.0939$ eV)

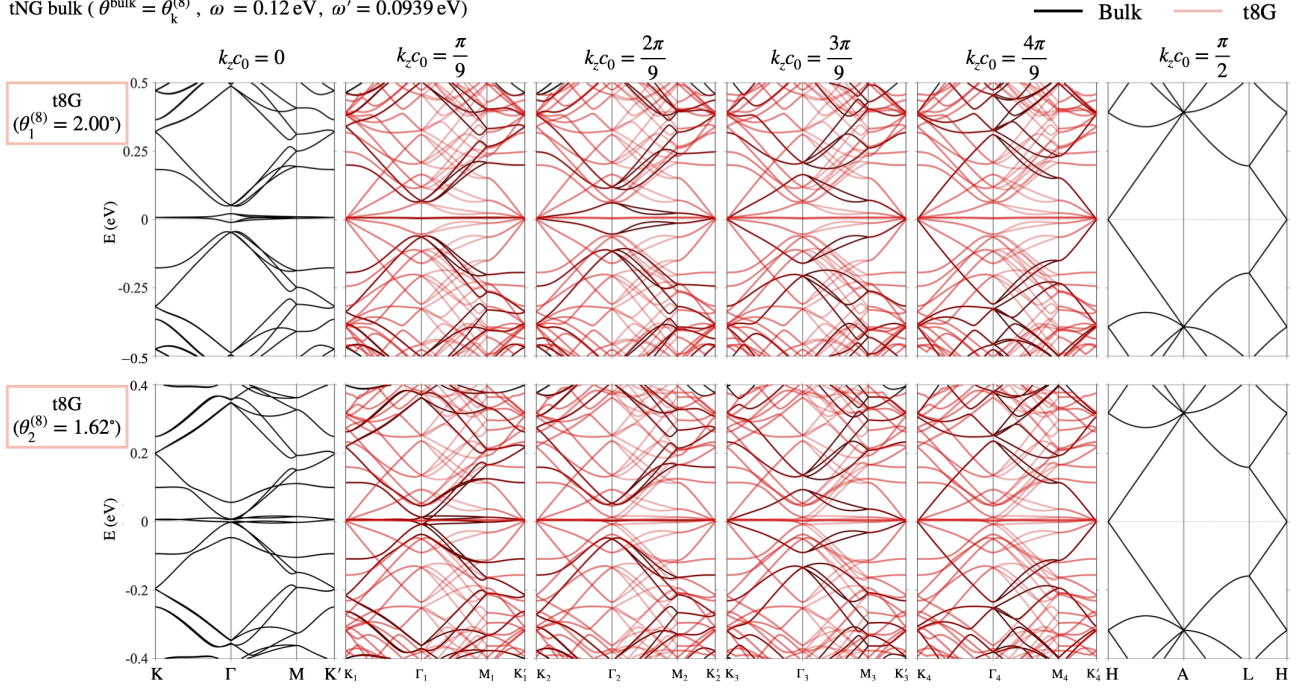


Figure D3. (color online) Bulk (black) and t8G (red) electronic band structures using the continuum model where we tune $\theta_1^{(8)} = 2.00^\circ$, and $\theta_2^{(8)} = 1.62^\circ$ to the first and second magic angle of t8G, and $\theta^{\text{bulk}} = \theta_k^{(8)}$ for the bulk. Similar to Fig. 5, this allows us to probe both the first and second magic angle in the K, Γ, M, K' plane where in both cases the bulk to finite mapping matches reasonably well. The tunneling amplitudes used for ω and ω' are the same in Fig. 3, and the height of a unit cell of the bulk in z -direction is $2c_0$.